

Machine-learning based interatomic potential for amorphous carbon

Volker L. Deringer^{1,2,*} and Gábor Csányi¹

¹*Engineering Laboratory, University of Cambridge, Trumpington Street, Cambridge CB2 1PZ, UK*

²*Department of Chemistry, University of Cambridge, Lensfield Road, Cambridge CB2 1EW, UK*

(Dated: February 2, 2022)

We introduce a Gaussian approximation potential (GAP) for atomistic simulations of liquid and amorphous elemental carbon. Based on a machine-learning representation of the density-functional theory (DFT) potential-energy surface, such interatomic potentials enable materials simulations with close-to DFT accuracy but at much lower computational cost. We first determine the maximum accuracy that any finite-range potential can achieve in carbon structures; then, using a novel hierarchical set of two-, three-, and many-body structural descriptors, we construct a GAP model that can indeed reach the target accuracy. The potential yields accurate energetic and structural properties over a wide range of densities; it also correctly captures the structure of the liquid phases, at variance with state-of-the-art empirical potentials. Exemplary applications of the GAP model to surfaces of “diamond-like” tetrahedral amorphous carbon (*ta*-C) are presented, including an estimate of the amorphous material’s surface energy, and simulations of high-temperature surface reconstructions (“graphitization”). The new interatomic potential appears to be promising for realistic and accurate simulations of nanoscale amorphous carbon structures.

I. INTRODUCTION

Carbon is among the most intriguing elements due to its structural diversity, and its solid-state forms range from diamond and graphite via many more complex allotropes^{1–3} onward to amorphous phases (*a*-C). The atomic structures of *a*-C samples depend strongly on density and are characterized by the coexistence of threefold (“sp²”) and fourfold bonded (“sp³”) carbon atoms. In this sense, low- and high-density forms of *a*-C are loosely reminiscent of graphite and diamond, respectively, but the actual situation is much more complex (Fig. 1). “Tetrahedral amorphous” carbon (*ta*-C), the dense, sp³-rich form, is of particular technological interest due to its attractive mechanical properties.^{4–6}

Atomistic simulations have long been providing useful insight into *a*-C materials.¹⁰ Many empirical interatomic potentials exist for carbon, from the original Tersoff¹¹ and Brenner¹² formulations to more recent developments, including an environment-dependent interaction potential (EDIP),¹³ improved reactive bond-order (REBO) potentials,^{14,15} or a recently re-parametrized reactive force field (ReaxFF);¹⁶ a comprehensive comparative study of such potentials was very recently carried out.⁸ These fast potentials make large-scale molecular-dynamics (MD) simulations possible, and have been applied to engineering problems such as fracture¹⁷ or friction and wear of *ta*-C coatings;¹⁸ they are efficient enough to perform thin-film deposition simulations,¹⁹ thus directly mirroring the atomic-scale processes in experiments. Nonetheless, these potentials remain empirical in nature, and may have serious shortcomings: prominent examples are an underestimated concentration of sp³-bonded atoms in *ta*-C,¹⁵ and poor description of surfaces. A general problem of empirical potentials is the inevitable compromise in accuracy for predicting different material properties.

On the other hand, seminal studies based on tight-

binding schemes^{20–22} as well as density-functional theory (DFT)^{23–26} early on afforded atomistic structure models of *a*-C, and more recent DFT-MD studies dealt with applications in photovoltaics²⁷ or coatings.²⁸ Furthermore, liquid carbon has been of interest—for example, in first-principles studies of the diamond melting line which is difficult to evaluate experimentally.²⁹ Despite their usefulness, however, DFT-based methods are limited to quite small system sizes, and even with the computational power available nowadays, they are limited in practice to a few hundred atoms. This makes many of the above scenarios simply inaccessible to predictive DFT-quality simulations.

To bridge the long-standing gap between these two realms, a novel class of simulation methods has recently emerged which is based on machine learning (ML). The key idea is to map a set of atomic environments *directly* onto numerical values for energies and forces; these quantities are “trained” from a large and accurate quantum-mechanical reference database but subsequently interpolated using the ML algorithm. If training is successful, this makes atomistic simulations close to quantum-mechanical accuracy accessible but requires less computational effort by many orders of magnitude. Recent implementations use high-dimensional artificial neural networks,^{30–32} compressed sensing,³³ or Gaussian process regression.³⁴ Interatomic ML-based potentials have been developed for several prototypical solids^{30–39} and applied, *e.g.*, in studies of phase transitions.⁴⁰ We mention in passing that ML schemes are currently being developed to estimate other fundamental properties of molecules and solids, including atomization energies,⁴¹ multipolar polarization,⁴² band gaps,⁴³ or NMR parameters.⁴⁴ A recent tutorial review of the field is in Ref. 45.

Previous ML potentials have been created for the crystalline carbon allotropes diamond and graphite,^{34,36} but as those were trained on a small region of configuration space, they are not suitable for simulating *a*-C. In-

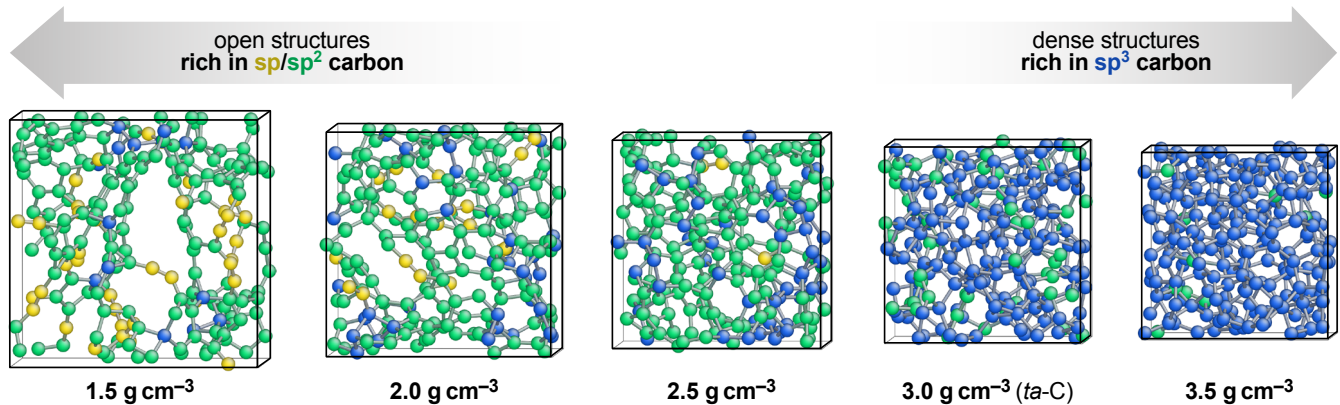


FIG. 1. Exemplary *a*-C structures at various densities, obtained in 216-atom cells from DFT melt-quench simulations. Note the gradual transition from open to dense networks, and the coexistence of twofold (“sp”; yellow), threefold (“sp²”; green), and fourfold (“sp³”; blue) coordinated carbon atoms. The open, low-density structures are metastable and on much further annealing will form more sp²-rich networks;^{7,8} here, on purpose, we focus on the as-quenched structures shown, to assess as diverse local environments as possible. Bonds are drawn up to a maximum interatomic distance of 1.85 Å, and coordination numbers are determined using the same cutoff. Structures were visualized using ATOMEYE.⁹

deed, the only reported ML potential dealing with amorphous matter is a neural-network potential for the phase-change data-storage material GeTe⁴⁶ that enabled large-scale simulations of thermal transport⁴⁷ and atomistic processes during crystallization.⁴⁸ Amorphous materials are structurally much more diverse than their crystalline counterparts, and despite the lack of long-range translational symmetry, their properties depend crucially on structural order on the local and intermediate length scales.⁴⁹ The required large unit cells and the long relaxation times make it very difficult to use DFT simulations for amorphous materials of practical interest.^{46,50} The latter are hence particularly promising targets for high-quality ML potentials.

In this work, we introduce an interatomic Gaussian approximation potential (GAP) for condensed-phase elemental carbon, with particular focus on liquid and amorphous phases of various densities. First, we systematically determine the maximum accuracy that any finite-range interatomic potential for carbon can achieve as a function of its neighbor cutoff, independently of how it is fitted. Then, we show that our GAP does indeed reach this accuracy, and furthermore provides reliable structural and topological data that agree well with the computationally much more demanding DFT benchmarks. Finally, we show predictions for energies and structures of *ta*-C surfaces, which play a key role in fracture and wear processes.

II. THEORY

The Gaussian approximation potential (GAP)^{34,51} is an ML approach to atomistic materials modeling, whereby an interatomic potential for the given material is “trained” from a database of reference quantum-

mechanical data, and is then used to interpolate energies and forces for arbitrary structures. In order to make simulation of large systems feasible, the total energy is broken down into a sum of local contributions, given by an local energy function ε . This function is expanded in a basis set adapted to the input database; it is generated using a kernel function, or similarity measure of neighbor environments. The choice of this kernel (and the symmetries it obeys) is critical for the success of any ML potential.⁵²

Previous ML potentials for solids used a decomposition into atomic energies, and employed many-body descriptors to represent the atomic neighbor environment—comprising all neighbors of an atom up to a given cutoff radius.^{34,53–56} However, for a complete description of these atomic environments one must fit the atomic energy function in a high-dimensional space. This leads to poor “extrapolation”, that is, to a poor fit in regions of configuration space far away from any data points. A long simulation will likely find such regions—especially at high temperatures, and/or when disorder is large. Indeed, in the present case of *a*-C, we encountered problems early during training when using a single many-body descriptor only: MD runs driven by such GAP models showed atoms aggregating at unreasonably small (sub-Å) distances. This is a very general challenge during the development of high-dimensional ML potentials, which carry the risk of erroneous extrapolation behavior unless carefully tested and used.

In this work, we generalize the many-body GAP approach for solids: we retain the many-body terms but augment them with two- and three-body “descriptors”—distances between atoms and angles in triplets. The latter terms hence represent two- and three-body interactions as in traditional (empirical) interatomic potentials, but now all descriptors and associated local-energy con-

tributions are part of the same ML framework. Our starting point is thus the following expression for the total energy:

$$E = \left(\delta^{(2b)}\right)^2 \sum_{i \in \text{pairs}} \varepsilon^{(2b)}(\mathbf{q}_i^{(2b)}) + \left(\delta^{(3b)}\right)^2 \sum_{j \in \text{triplets}} \varepsilon^{(3b)}(\mathbf{q}_j^{(3b)}) + \left(\delta^{(\text{MB})}\right)^2 \sum_{a \in \text{atoms}} \varepsilon^{(\text{MB})}(\mathbf{q}_a^{(\text{MB})}) \quad (1)$$

where “2b”, “3b”, and “MB” denote two-, three-, and many-body interactions, respectively. This is similar in spirit to the recently introduced Moment Tensor Potentials,⁵⁶ and also to another scheme that uses a parametric two-body term in combination with a neural network that describes the many-body interactions⁵⁷.

In the above expression, the δ are scaling parameters, and each corresponds to the distribution of energy contributions a given interaction term has to represent. We choose the largest value for the 2b terms, which describe the largest share of the total energy; on top of that, we add a 3b term, and finally the many-body term with the smallest $\delta^{(d)}$.

The local energy corresponding to each descriptor $d \in \{2b, 3b, \text{MB}\}$ is given by a linear combination of kernel functions³⁴

$$\varepsilon^{(d)}(\mathbf{q}^{(d)}) = \sum_{t=1}^{N_t^{(d)}} \alpha_t^{(d)} K^{(d)}(\mathbf{q}^{(d)}, \mathbf{q}_t^{(d)}), \quad (2)$$

where t denotes one of N_t training configurations \mathbf{q}_t , each of which attains a weighting coefficient α_t during fitting, and K is a covariance kernel which quantifies how similar the input configuration \mathbf{q} is to the t -th training configuration, \mathbf{q}_t . In practice, we sparsify the representation and only allow the sum to range over a number of “representative points” drawn from the full training database ($N_t \ll N_{\text{full}}$). The number of representative points differs for each descriptor and must be carefully controlled during training.

Both for 2b and 3b contributions, we use a squared exponential kernel,³⁴

$$K^{(d)}(\mathbf{q}_i^{(d)}, \mathbf{q}_t^{(d)}) = \exp \left[-\frac{1}{2} \sum_{\xi} \frac{(q_{\xi,i}^{(d)} - q_{\xi,t}^{(d)})^2}{\theta_{\xi}^2} \right], \quad (3)$$

where ξ is an index running over the components of the descriptor vector $\mathbf{q}^{(d)}$. In the case of pairs, the descriptor has one single scalar component (namely, the distance r_{12} between the two atoms involved):

$$q^{(2b)} = |\mathbf{r}_2 - \mathbf{r}_1| \equiv r_{12}; \quad (4)$$

for triplets, we do not directly use the natural coordinates r_{12} , r_{13} , and r_{23} , but a different form to enforce symmetry

over permutation of the neighbor atoms 2 and 3:⁵¹

$$\mathbf{q}^{(3b)} = \begin{pmatrix} r_{12} + r_{13} \\ (r_{12} - r_{13})^2 \\ r_{23} \end{pmatrix}. \quad (5)$$

Note that with this choice of descriptors, the first term in Eq. 1 is equivalent to a pair potential, and the second is a generic three-body potential, but in the GAP framework both do not impose constraints on the specific functional form.

For the many-body term, we use the recently introduced Smooth Overlap of Atomic Positions (SOAP)⁵² descriptor, which has proven successful in generating GAP models for tungsten,³⁹ in classifying diverse molecular and solid-state structures,⁵⁸ and very recently in constraining structural refinements of amorphous Si.⁵⁹ We briefly review the most pertinent features; detailed formulae and derivations are in Ref. 52. SOAP starts from the neighborhood density of a given atom a , defined as

$$\rho_a(\mathbf{r}) = \sum_b \exp \left[-\frac{(\mathbf{r} - \mathbf{r}_{ab})^2}{2\sigma_{\text{at}}^2} \right] \times f_{\text{cut}}(r_{ab}), \quad (6)$$

where the sum is over neighboring atoms, and the cut-off function f_{cut} , which ensures compact support, goes smoothly to zero at r_{cut} over a characteristic width r_{Δ} . The parameter σ_{at} ultimately controls the smoothness of the potential. The neighbor density is expanded into a local basis of orthogonal radial basis functions g_n and spherical harmonics Y_{lm} ,

$$\rho_a(\mathbf{r}) = \sum_{nlm} c_{nlm}^{(a)} g_n(r) Y_{lm}(\hat{\mathbf{r}}), \quad (7)$$

and the expansion coefficients are used to form the spherical power spectrum,

$$p_{nn'l}^{(a)} = \sqrt{\frac{8\pi^2}{2l+1}} \sum_m \left(c_{nlm}^{(a)} \right)^* c_{n'l m}^{(a)}, \quad (8)$$

which is invariant both to permutations over neighbors and to 3D rotations of the neighbor environment. We use the elements of a finite truncation of the power spectrum (up to $n \leq n_{\text{max}}$ and $l \leq l_{\text{max}}$) as components of the many-body descriptor vector $\mathbf{q}_a^{(\text{MB})}$, which furthermore is normalized to have unit length.

The kernel function for the SOAP term is the simple dot product,

$$k(\mathbf{q}_a^{(\text{MB})}, \mathbf{q}_t^{(\text{MB})}) = \sum_{nn'l} p_{nn'l}^{(a)} p_{nn'l}^{(t)} = \mathbf{q}_a^{(\text{MB})} \cdot \mathbf{q}_t^{(\text{MB})}, \quad (9)$$

and we find it advantageous to raise it to a small integer power for a sharper distinction between different environments. This gives the final kernel

$$K^{(\text{MB})}(\mathbf{q}_a^{(\text{MB})}, \mathbf{q}_t^{(\text{MB})}) = \left| \mathbf{q}_a^{(\text{MB})} \cdot \mathbf{q}_t^{(\text{MB})} \right|^{\zeta}. \quad (10)$$

This dot product kernel is a natural choice to use with the power spectrum descriptor, as it makes the kernel equivalent (up to normalization) to the integrated overlap of the original neighbor densities,

$$\int d\hat{R} \left| \int \rho_a(\mathbf{r}) \rho_t(\hat{R}\mathbf{r}) \right|^2. \quad (11)$$

The expression for the total energy in our GAP model is therefore given by

$$\begin{aligned} E = & \left(\delta^{(2b)} \right)^2 \sum_i \sum_t \alpha_t^{(2b)} K^{(2b)} \left(\mathbf{q}_i^{(2b)}, \mathbf{q}_t^{(2b)} \right) \\ & + \left(\delta^{(3b)} \right)^2 \sum_j \sum_t \alpha_t^{(3b)} K^{(3b)} \left(\mathbf{q}_j^{(3b)}, \mathbf{q}_t^{(3b)} \right) \\ & + \left(\delta^{(MB)} \right)^2 \sum_a \sum_t \alpha_t^{(MB)} K^{(MB)} \left(\mathbf{q}_a^{(MB)}, \mathbf{q}_t^{(MB)} \right), \end{aligned} \quad (12)$$

where all fitting coefficients α enter linearly, and therefore we can obtain them simply using linear algebra. This is in contrast with the difficult nonlinear parameter optimization required both for traditional interatomic potentials and for some other ML schemes, e.g., artificial neural networks.

The above discussion does not include the prescription for obtaining the linear fitting coefficients. In practice, this is complicated due to the fact that the quantum mechanical data is only available in the form of *total* energies, atomic forces, and virial stresses. The full formalism simultaneously includes sparsification, multiple energy terms, and fitting to total energies and their derivatives; is given elsewhere.⁵¹

To illustrate the role of the combined descriptors, we use different (and increasingly complex) GAP models to compute the potential-energy curve for an isolated carbon dimer; these models have been fitted to the full bulk and surface training set described below that additionally incorporates DFT data points between 0.8 and 3.7 Å in small increments. The results are summarized in Fig. 2: GAP models using 2b descriptors only, or a combination of 2b+3b, reproduce the minimum and the repulsion at small C–C distances reasonably well, but the longer-range behavior is not yet correctly described. An interesting result is seen when using a many-body descriptor *only*: the fit is very good for the region where data points are provided (blue circles), but shows unphysical behavior at $r < 0.8$ Å; this can, and will, then lead to bad extrapolation in practical simulations. By contrast, a GAP model combining all three descriptors (Eq. 12) gives a highly satisfactory result (red line in Fig. 2).

III. COMPUTATIONAL METHODS

A. General protocol for melt–quench simulations

Structural data were obtained from melt–quench MD, following protocols that are well established for *a*-C.^{23,25}

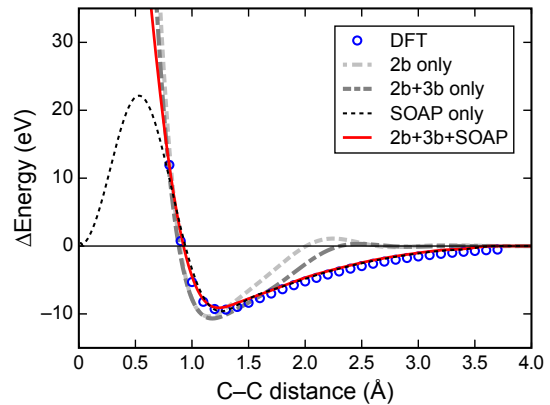


FIG. 2. Potential-energy scans for an isolated carbon dimer. This plot, with DFT data as reference (blue), allows us to assess the use of different structural descriptors: all three combined are needed for a high-quality fit (see text).

Initial simulations were performed in the DFT framework, subsequent ones with GAP, but both employed the same temperature protocol. For each simulation, an (unstable) simple-cubic lattice of carbon atoms was generated at the appropriate density and held at a constant temperature of 9000 K for 3 ps. The simulation cell was then held in the liquid state at 5000 K (3 ps), quenched with an exponentially decaying temperature profile (0.5 ps), and finally annealed at 300 K (3 ps). The timestep was 1 fs in all MD simulations.

B. DFT-based (“*ab initio*”) molecular dynamics

Structures for initial training, as well as benchmarks for *a*-C properties, were generated using DFT-based *ab initio* MD, using the QUICKSTEP scheme and a stochastic Langevin thermostat⁶⁰ as implemented in CP2K.^{61,62} Electronic wavefunctions were described at the Γ point using a mixed-basis scheme with Goedecker–Teter–Hutter pseudopotentials⁶³ and a cutoff energy of 250 Ry. Double- ζ quality basis functions were used for the carbon 2s and 2p levels.

Exchange and correlation were treated in the local density approximation (LDA),⁶⁴ both during *ab initio* MD and training-data generation. This functional, despite its simplicity, has long been used for atomistic simulations of *a*-C and is still the *de facto* standard for many current applications.^{15,27,28} Further work may be concerned with the application of higher-level DFT methods, such as computationally much more expensive hybrid functionals, or the implementation of dispersion corrections—these will likely be interesting additions to the GAP framework, but are beyond the scope of the present study.

C. Construction of the training database

Our training database contains structural snapshots from *ab initio* MD and also, as it is iteratively extended, from GAP-driven simulations. No matter how generated, all structures are then subjected to single-point DFT-LDA computations, to yield well-converged energies and forces for training. This was done using CASTEP,⁶⁵ with dense reciprocal-space meshes (maximum spacing 0.03 \AA^{-1}),⁶⁶ a 650 eV cutoff for plane-wave expansions, and an extrapolation scheme to counteract finite-basis errors.⁶⁷ Gaussian smearing of 0.1 eV width was applied to electronic levels. The halting criterion for SCF iterations was $\Delta E < 10^{-8} \text{ eV}$.

Initial training data were computed for snapshots from *ab initio* MD melt-quench trajectories, and a preliminary GAP was fitted to those data. The resulting potential reproduced the structure of the 9000 K liquid well, that of the 5000 K liquid satisfactorily, but not yet that of the amorphous phase. In retrospect, this is easily understood: the 9000 K liquid is highly diffusive, and so one single 3 ps trajectory apparently contains sufficiently different atomic environments to sample configuration space during training. A quenched amorphous structure, by contrast, is essentially one single snapshot with thermal fluctuations but no major changes in connectivity. Training from DFT data alone would thus incur significant expense, as each uncorrelated *a*-C sample would require a *full* melt-quench trajectory (9500 steps) of which only the last snapshot were of use.

Instead, an initial GAP was used to generate liquid structures at 5000 K, which were then briefly re-equilibrated (500 steps) and quenched (500 steps) using *ab initio* MD. This was done for ten uncorrelated structures each at 2.0, 3.0, 3.25, and 3.5 g cm^{-3} , thus placing more emphasis on high-density amorphous phases which are richer in tetrahedral (“sp³”) motifs and thus structurally most different from the liquids.

The resulting, amended database was used to train a new GAP, which was further extended iteratively by performing melt-quench simulations *fully* driven by the previous GAP version, as is common practice in the development of ML potentials.^{39,46} Thereby, all GAP-MD simulations were carried out using a Langevin thermostat as implemented in **quippy** (www.libatoms.org), and the same temperature profiles as in the **cp2k** simulations. A typical protocol included the generation of 100 independent structures at densities of $1.5\text{--}3.5 \text{ cm}^{-3}$, with system sizes of 27–125 atoms. For one or more snapshots from each trajectory, a single-point DFT computation was performed and the results were included in the next round of training.

To add amorphous surfaces to the training set, we generated *ta*-C structures using GAP, and from these created slabs by adding vacuum regions. In parallel *ab initio* MD runs, amorphous slabs were briefly heated at up to 5000 K, and structures from both procedures were added to the database. We reiterate that it is not

TABLE I. Key parameters for the GAP model created in this work (see Sec. II for definitions).

	2-body	3-body	SOAP
$\delta \text{ (eV)}^a$	5.0	0.3	0.1
$r_{\text{cut}} \text{ (\AA)}$	3.7	3.0	3.7
$r_{\Delta} \text{ (\AA)}$			0.5
$\sigma_{\text{at}} \text{ (\AA)}$			0.5
$n_{\text{max}}, l_{\text{max}}$			8
ζ			4
Sparsification	Uniform	Uniform	CUR
$N_t \text{ (a-C bulk)}$		125	2500
$N_t \text{ (a-C surfaces)}$		50	1000
$N_t \text{ (crystalline)}$		25	500
$N_t \text{ (dimer)}$			30
$N_t \text{ (total)}$	15	200	4030

^aFor the 2b and 3b descriptors, when specifying training input, the δ given here is divided by the expected number of pairs or triplets an atom is involved in.

problematic to generate the training *structures* with different techniques,⁶⁸ as their *energies and forces* are re-computed using the same reference method (tightly converged plane-wave DFT).

Once the training database of liquid and amorphous structures had been generated, it was further extended by including randomly distorted unit cells of the crystalline allotropes, diamond and graphite. This combined database was then split into a training and a test set (90:10); the latter was not included in the fit but used for validation. Finally, DFT data for an isolated dimer were added (cf. Fig. 2). A full description of the training database is provided as Supplementary Information.

D. GAP model fitting

Values for the above GAP parameters as used in the present work are given in Table I. Furthermore, the regularization parameters of the Gaussian process corresponding to the expected errors were as follows. For liquid and amorphous structures we set 0.002 eV (energies) and 0.2 eV \AA^{-1} (forces); for the crystalline forms, we multiplied both values by 0.1, and additionally included virials in the training, with an expected error of 0.2 eV. Sparsification was done with the CUR method⁶⁹ for the SOAP kernel, whereas a simple uniform grid of basis function locations was used for the 2b and 3b terms. In the following, unless specified otherwise, “GAP model” refers to one with all three terms (2b, 3b, and SOAP). The potential files are freely available at <http://www.libatoms.org>.

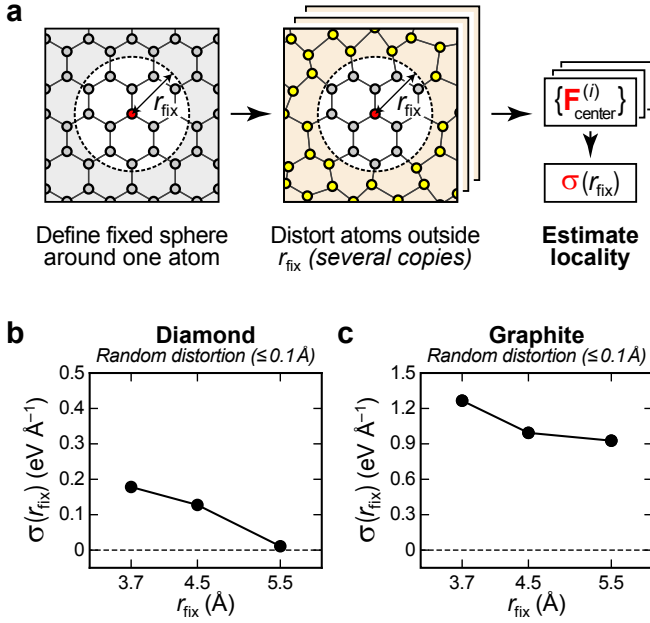


FIG. 3. (a) Schematic overview of the procedure used here for locality tests. (b,c) Results for diamond and graphite, respectively, obtained by displacing all atoms outside r_{fix} randomly by up to 0.1 Å and inspecting the standard deviation of the force on the central atom.

IV. RESULTS AND DISCUSSION

A. Locality and target accuracy

A central assumption of all interatomic potentials is that of *locality*: the energy associated with a given atom or bond depends on its immediate environment ($\varepsilon_i \equiv \varepsilon(\mathbf{q}_i)$), but not on atoms further away than a given cut-off radius (ignoring electrostatic terms and van der Waals corrections for the moment). A similar assumption follows directly for the forces on atoms. While this approximation is often made implicitly, and tacitly, in the development of empirical potentials, their ML-based counterparts aim at *quantitative* energy and force accuracy with respect to the reference potential-energy surface, and so at the outset we must numerically determine how well the above assumption holds. This question is very general, and likely relevant beyond the present study.

Quantum-mechanical models such as DFT are inherently nonlocal: they do not allow for a unique partitioning of the total energy into a sum of local terms. Nonetheless, quantum models of electronic structure are *nearsighted*,⁷⁰ which means that the reduced one-particle density matrix decays strongly (at least under the assumption of screening, for insulators, and in general at finite temperature).⁷¹ This implies locality in the atomic forces, which we quantify as the decay of the dependence of an atomic force on a neighboring atom's position as the distance between the two atoms grows. A direct manifestation of this is the decay of the dynamical matrix or

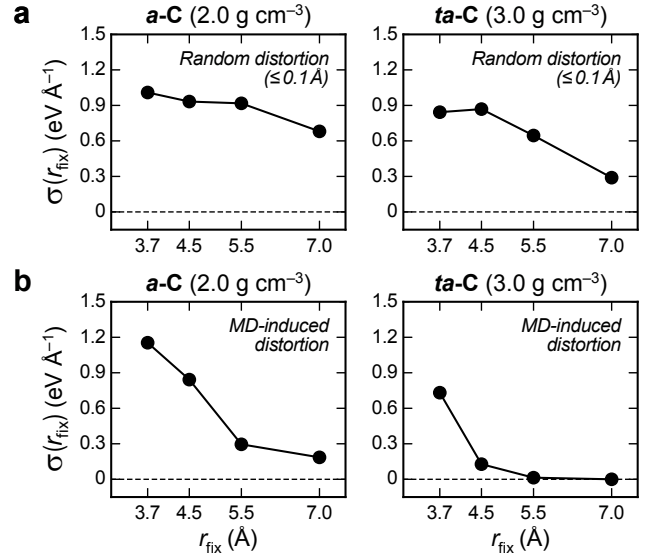


FIG. 4. Locality tests for *a*-C structures. (a) Force locality in low- and high-density forms, evaluated in the presence of a small distortion that preserves the major topological features of the amorphous network. In both panels, data have been collected over three structural models; for each, ten atoms were randomly sampled as sphere centers, and five independent distortions were created for each central atom. (b) Same but for a large distortion induced by MD at very high temperature such as to erase any structural memory of the initial cell outside the fixed sphere.

Hessian.

Using our reference quantum-mechanical method, we can calculate the above decay of the dependence of the atomic forces, and thus determine a bound on force locality. Conversely, this gives a bound on the force accuracy of *any* interatomic potential model based on a local energy decomposition. We stress again that all this applies only for materials without strong polar interactions—or for models from which such polar interactions have been substantially subtracted.

The procedure, as previously employed by Bartók *et al.*,³⁴ is sketched in Fig. 3a: we select one atom in a given simulation cell and define a sphere of radius r_{fix} around this atom in that the atoms are fixed. We then create many structures which differ in the positions of the atoms *outside* the fixed sphere, and for each calculate the force on the central atom using DFT.⁷² Locality is then characterized by plotting the standard deviation of this force as a function of r_{fix} .

We first consider the crystalline allotropes and begin by introducing rather modest distortions, moving all atoms outside r_{fix} randomly by up to 0.1 Å . Diamond exhibits strong locality (Fig. 3b): the overall force deviations due to displacements outside the spheres are small, and they gradually vanish and are practically zero at $r_{\text{fix}} = 5.5 \text{ Å}$. Graphite, by stark contrast, is highly non-local (Fig. 3c): the force deviations are much larger than

in diamond, and they do not decay as rapidly.

Turning now to the locality in amorphous carbon, we focus on two representative densities: a low-density form (2.0 g cm^{-3}) and an approximant of dense *ta*-C (3.0 g cm^{-3}), and again we start by randomly displacing atoms by up to 0.1 \AA (Fig. 4a). Qualitatively, the results seem to be in line with those for the crystalline phases: the more sp^2 -rich form (2.0 g cm^{-3}) clearly shows lower locality.⁷³ Due to the coexistence of sp^2/sp^3 motifs in the amorphous forms, however, there is no clear-cut distinction between the two system sizes, and *ta*-C retains a notable degree of nonlocality.

The displacements so far have perturbed the atoms outside r_{fix} , but the models still retain a “memory” of the initial structure even outside the fixed sphere. We therefore next perform Tersoff MD,¹¹ starting with velocities that correspond to a very high temperature, and let the system evolve for 1 ps, again keeping the central sphere fixed. This leads to a more local picture (Fig. 4b), especially for the dense “diamond-like” form; nonetheless, the overall $\sigma(3.7 \text{ \AA})$ values in the latter are much larger than in the crystalline form.

Summarizing, diamond shows the strong force locality expected for a covalent semiconductor; graphite, by contrast, is highly nonlocal. The latter holds for the amorphous phases as well, more pronounced so at low density. As a ballpark measure, for an α -C potential with a cutoff radius of 3.7 \AA , we estimate the lowest achievable standard deviation of force components to be $\approx 1 \text{ eV \AA}^{-1}$ (Fig. 4). One might increase r_{cut} up to 7.0 \AA , which is expected to lower the standard deviation to $\approx 0.7 \text{ eV \AA}^{-1}$, but the tradeoff in terms of much greater computational expense (both during training and application of the GAP) does not seem to justify this. Hence, all that follows will be done in the framework of modest r_{cut} values as given in Table I.

B. Energies and forces

With the target errors for a finite-range potential established, we can now analyze the quality of our GAP. We therefore test how much the predicted energies and forces deviate from DFT reference values. Again, we assess different combinations of structural descriptors, and thereby illustrate how hierarchical GAP models can achieve increasing accuracy. Correlation plots of energies and force components already make this clear (Fig. 5a): using the 2b descriptor only, there is a certain degree of correlation between the DFT and GAP energies, but with much scatter, and there is essentially no correlation between DFT and GAP force components (light gray). A 2b+3b model is clearly better (dark gray), but ultimately SOAP must be added (red) to achieve the accuracy limit imposed by nonlocality (Fig. 5b). Figure 5c shows the errors as cumulative distributions: the curves move left (toward lower errors) and up (to a higher degree of confidence) as successively more complex descriptors

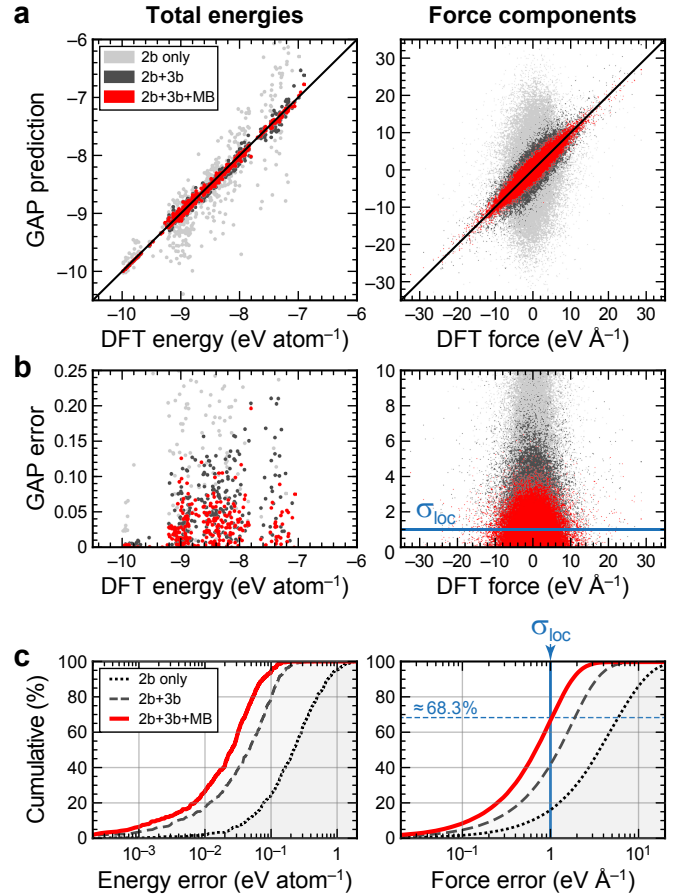


FIG. 5. (a) Scatterplots of DFT-computed and GAP-predicted total energies (*left*; relative to a free singlet atom) and force components (*right*) on a test set of 450 configurations. Results are shown for hierarchical GAP models with different combinations of descriptors (Sec. II). (b) Absolute errors of the respective quantities, similarly resolved according to different sets of descriptors. For the force components (*right*), akin to Ref. 34, an estimate of the maximum achievable standard deviation as judged from locality tests (Sec. IV A) is indicated by a blue line. (c) Cumulative distributions: a given point (x, y) on the curve indicates that y percent of all structures have an error equal to or below x . The standard deviation estimated from locality tests, σ_{loc} , which should enclose $\approx 68.3\%$ of the GAP force component errors, is indicated in blue: indeed, the GAP model with combined 2b, 3b, and MB descriptors (red line) does reach this accuracy.

are added to the GAP model.

For such a heterogeneous training database, it is interesting to further break down the GAP’s performance according to configuration types: slightly distorted diamond configurations will be easier for an ML potential to fit than disordered liquid carbon. Indeed, looking back at Fig. 5 shows that the training points with lowest overall energy show the lowest fitting errors; these are precisely the crystalline structures.

In Fig. 6, we show the distribution of errors for configurations coming from different stages of the melt–quench

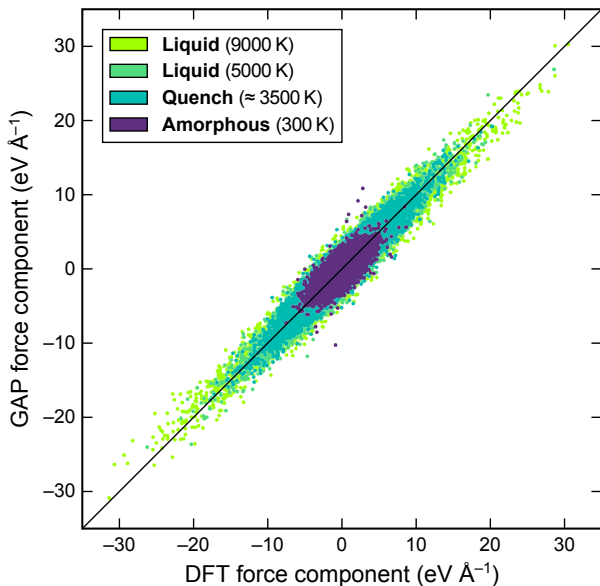


FIG. 6. DFT-computed versus GAP-predicted force components in a set of 125-atom snapshots of liquid and amorphous carbon, emphasizing the overall magnitude of forces the GAP has to learn at various parts of the melt-quench trajectories.

cycles. We investigate a set of 100 uncorrelated *a*-C structures, with 125 atoms each and randomized densities over the range 1.5–3.5 g cm⁻³, created using GAP-MD and subsequently analyzed using DFT. From each melt-quench trajectory, we take one configuration at each key step—that is, one from the 9000 K and one from the 5000 K liquid, one during quenching, and the final one from the quenched amorphous sample. The force errors are very similar for all parts of the trajectory, but the *absolute* magnitude of forces is much different; hence, in *relative* terms, the GAP performs much better for forces in the liquid than in the amorphous phases. A detailed numerical analysis is in Table II. We estimate how widely the absolute DFT force components are distributed by giving their 95-th percentile value P_{95} . We then divide the GAP force component error by P_{95} ; the lower this ratio, the better. For melt-quench simulations, the situation appears favorable: as the structure is “frozen in” during quenching, the topology (say, the sp^3 count) of the amorphous phase is largely determined by a correct description of the liquid.

C. Structural properties

From energy and force evaluations, we now move on to probe physical properties as predicted by our GAP. Table III compares its performance to DFT reference data for the diamond structure. Here and in the following, we will also make comparison to a state-of-the-art empirical potential, namely, a screened variant of the Tersoff po-

TABLE II. Energy and force RMS errors of our GAP, computed for a set of 125-atom structures (cf. Fig. 6), and also for the crystalline structures from the test set. Percentile values P_{95} for the absolute DFT values are given; these measure the range of data the GAP has to “learn”.

	Energy	Force components		
	(eV)	(eV Å ⁻¹)		
	RMS	RMS	P_{95}	Ratio
	(GAP)	(GAP)	(DFT)	
Liquid (9000 K)	0.041	1.27	6.52	0.19
Liquid (5000 K)	0.031	1.12	5.68	0.20
Quench	0.023	1.07	5.06	0.21
Amorphous	0.018	0.94	2.23	0.42
Crystalline	0.002	0.10	1.32	0.08

TABLE III. Structural and elastic properties of diamond, computed using DFT-LDA and our GAP as well as the screened Tersoff potential from Ref. 74 (“scrT”).

	DFT	GAP	scrT
a (Å)	3.532	3.539	3.566
B_{Voigt} (GPa)	466	438	427
C_{11} (GPa)	1101	1090	1073
C_{12} (GPa)	148	112	104
C_{44} (GPa)	592	594	640

tential developed by Pastewka and coworkers.^{15,74} Similar potentials have been successfully applied in recent studies both to graphene⁷⁵ and to *ta*-C,⁷⁶ and are faster than GAP by about a factor of 50.

The lattice parameter a of diamond is accurately reproduced by the GAP; the bulk modulus and elastic constants are reasonable but deviate somewhat from the DFT reference (Table III). It was shown previously that a GAP model trained for the crystalline phases exclusively can reproduce the benchmark even better;³⁴ here, the gain in transferability (being able to model amorphous as well as crystalline phases) comes at a small price in terms of accuracy.

Similar tests for the graphite c parameter gave 6.625 Å (DFT) and 6.518 Å (GAP). Despite this slight overbinding (−1.6%), the agreement is appreciable, especially given that the Tersoff and Brenner potentials are short-ranged and cannot describe the interlayer spacing in graphite at all ($r_{\text{cut}} < c/2$).

We now turn to the main subject of the present work: the liquid and amorphous phases of carbon. We begin by inspecting the concentration of sp^3 atoms during melt-quench simulations (Fig. 7), and use this to once more assess the performance of different combined structural descriptors. The DFT reference (blue) shows that in liquid carbon at 3.0 g cm⁻³, approximately one-third of the atoms are in fourfold coordination, and this number increases strongly when quenching (6.0→6.5 ps in simula-

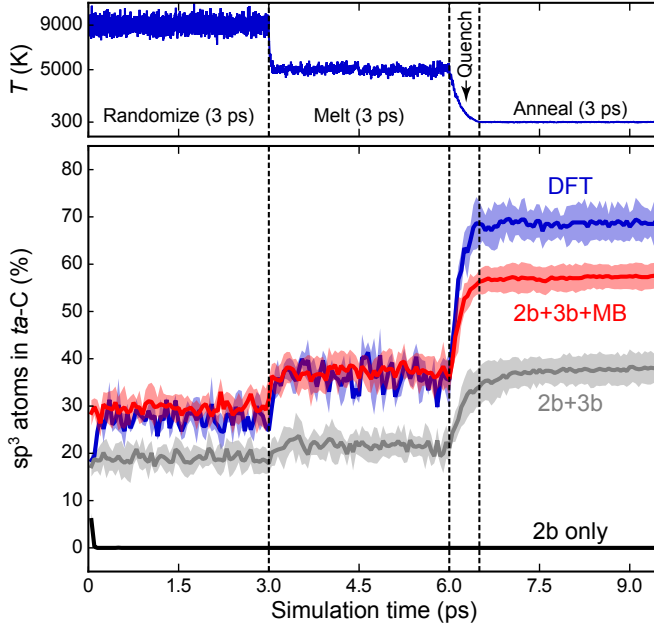


FIG. 7. *Top*: Exemplary temperature profile during a DFT-MD melt-quench simulation to yield a 216-atom structure of $ta-C$. *Bottom*: Concentration of sp^3 atoms during these cycles, measured by counting atomic neighbors up to a cutoff distance of 1.85 Å. DFT benchmarks are compared to GAP results using different combinations of descriptors; areas of light shading indicate standard deviations.

tion time). During annealing at 300 K, the DFT average then levels off at $\approx 70\%$; as only three structures were created with DFT, fluctuations and standard deviation (light blue shading) are sizeable. The GAP results, by comparison, clearly identify the need for combined structural descriptors when aiming to make physically meaningful predictions: using the two- and three-body descriptors only yields systematically too low sp^3 concentrations (gray), whereas both combined with SOAP essentially reproduce the DFT data for the liquid forms (red); the sp^3 count is still underestimated in the quenched amorphous phase. We performed additional GAP simulations in which we increased the quenching time from 0.5 to 2.0 ps, but this did not further improve the result. For completeness, we include in Fig. 7 results for a GAP model that employs two-body descriptors *only*—but in this case the atoms clump into unphysical structures within the first few steps (black line), not unexpectedly so.

The simplest measure of short-range order in a liquid or amorphous structure is given by the radial distribution function (RDF). In Fig. 8, we compare GAP results to those of DFT, and start by noting that both are very close. The liquid structures are more diffuse and less strongly ordered, and the RDFs show a nonzero first minimum at ≈ 1.9 Å, whereas the amorphous structures exhibit a gap between their first and second RDF peak. A small but visible asymmetry of the second RDF peak at ≈ 2 Å for all amorphous structures indicates the

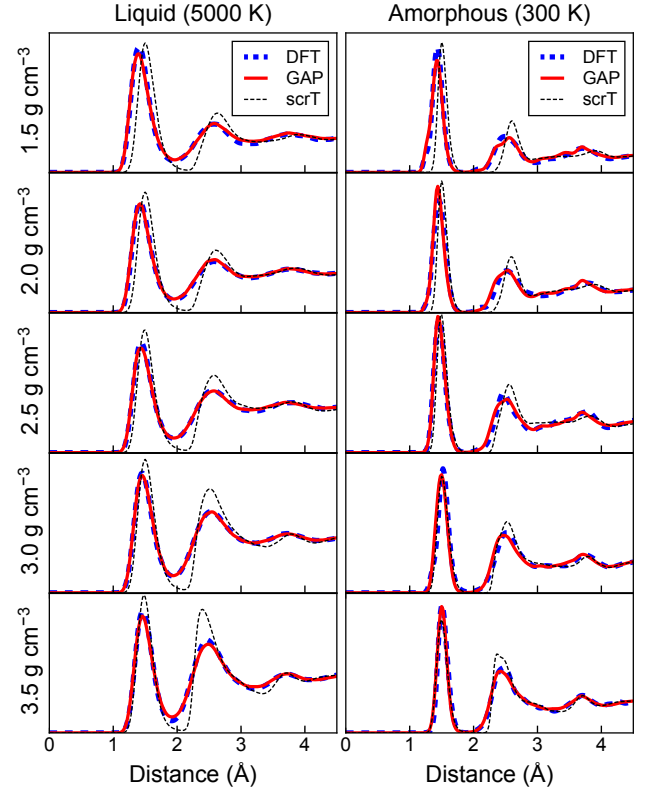


FIG. 8. Radial distribution functions for liquid (*left*) and subsequently quenched amorphous (*right*) carbon structures (ten independent 216-atom structures were created at each density). Results for five densities are given, spanning the entire range visualized in Fig. 1. “scrT” denotes the screened Tersoff potential as introduced in Ref. 74.

presence of fourfold rings. The screened Tersoff potential (“scrT”) does not predict the existence of such fourfold rings in $a-C$ (we will return to this below), and other than DFT and GAP it lowers the first RDF minimum to almost zero in all liquid structures.

Figure 9 shows angular distribution functions (ADFs). The ADF maxima at low (high) density are centered around 120° (109°), respectively, loosely mirroring the defining structural features of the crystalline allotropes (graphite honeycombs and diamond tetrahedra); naturally, this distribution is broader in the highly diffuse liquids than in the quenched amorphous structures. At low densities, a contribution close to 180° is seen in the DFT reference data, due to nearly linearly coordinated “sp” carbon atoms (yellow in Fig. 1); this is a minor feature at 2.5 and 2.0 g cm⁻³, but becomes prominent at 1.5 g cm⁻³, especially so in the quenched amorphous structures (top right panel in Fig. 9). The GAP reproduces these features very well, both the location and the extent of the maxima, as well as the overall shape of the ADF curves. The screened Tersoff potential deviates significantly from the DFT and GAP results, and the ADFs derived from it are zero both at 60° (absence of three-

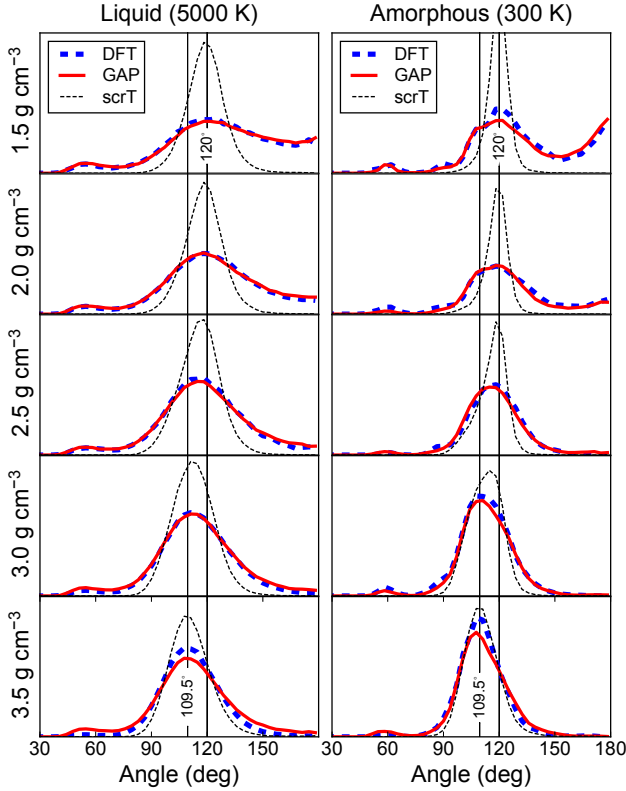


FIG. 9. As Fig. 8, but for angular distribution functions. Thin vertical lines mark angles of 109.5° and 120° , corresponding to ideal sp^3 (diamond-like) and sp^2 (graphite-like) motifs, respectively. The scaling of the vertical axes is arbitrary.

fold rings) and at 180° (absence of linear “sp-bonded” chains).

D. Coordination statistics and medium-range order

Among the key structural characteristics for a -C is the concentration of fourfold coordinated (“ sp^3 ”) atoms as function of the sample density. We assess this in Fig. 10, comparing GAP results to DFT but also to previous modeling and experimental studies. The empirical Brenner and Tersoff potentials, as is known,¹⁵ underestimate the sp^3 count at high density; indeed, one of the breakthrough successes of the screened Brenner and Tersoff potentials has been their much improved description of ta -C in this respect.¹⁵ In comparison, the GAP data (red in Fig. 10) are even closer to the DFT reference (blue), particularly at lower densities. The residual error of the GAP results is most pronounced at 3.0 g cm^{-3} , and so using this density for the example in Fig. 7 showed the worst of all cases.

Looking beyond the first nearest-neighbor shell, the medium-range order in amorphous materials is conventionally characterized by means of ring statistics, which we evaluate using Franzblau’s shortest-path algorithm.⁸⁰

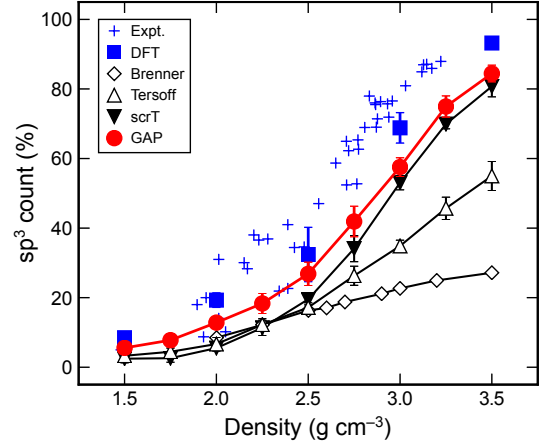


FIG. 10. Count of “ sp^3 ” (fourfold coordinated) carbon atoms in quenched a -C structures as a function of density. Ten independent melt-quench cycles were performed at each density for the empirical and GAP models; three independent ones were done for DFT. Data for the Brenner potential are taken from Ref. 15. Experimental data have been collected from Refs. 77–79. Error bars represent standard deviations. Lines between data points are only guides to the eye.

Again, we compare liquid and quenched amorphous structures side-by-side, and inspect the entire range from low to high densities (Fig. 11).

The DFT reference (blue) shows that the distribution is quite complex: at high densities, the ring sizes center around sixfold (similar to diamond, where $n = 6$ exclusively), and the distribution decays quickly beyond that; no large-membered rings are found in ta -C. By contrast, the distribution in the low-density structures is less clearly defined and does involve higher-order rings, indicative of structural voids.

The results for ta -C at 300 K are very similar with all three methods. In addition, the GAP model also recovers the three- and four-membered rings that are key features of the liquid and also prominent in low-density amorphous structures.²³ The screened Tersoff potential, by contrast, overestimates the average ring size in low-density a -C, and does not predict the occurrence of any three- or fourfold rings, neither in the liquid nor in the amorphous phases.

So far, all validation of the new potential has been done against DFT, and therefore necessarily been limited to rather modest system sizes of 216 atoms. The true strength of ML potentials, however, is in the application to larger structures. Figure 12 shows results for an 8,000-atom a -C structure at 1.5 g cm^{-3} , which would presently be impossible to generate with DFT-based MD even on state-of-the-art supercomputers.

RDFs and ADFs obtained with 216-atom and 8,000-atom structures are practically the same and are hence not shown. The situation for the ring statistics (Fig. 12b) is more complex. For small- and medium-sized rings, results for the large system (purple) come very close to

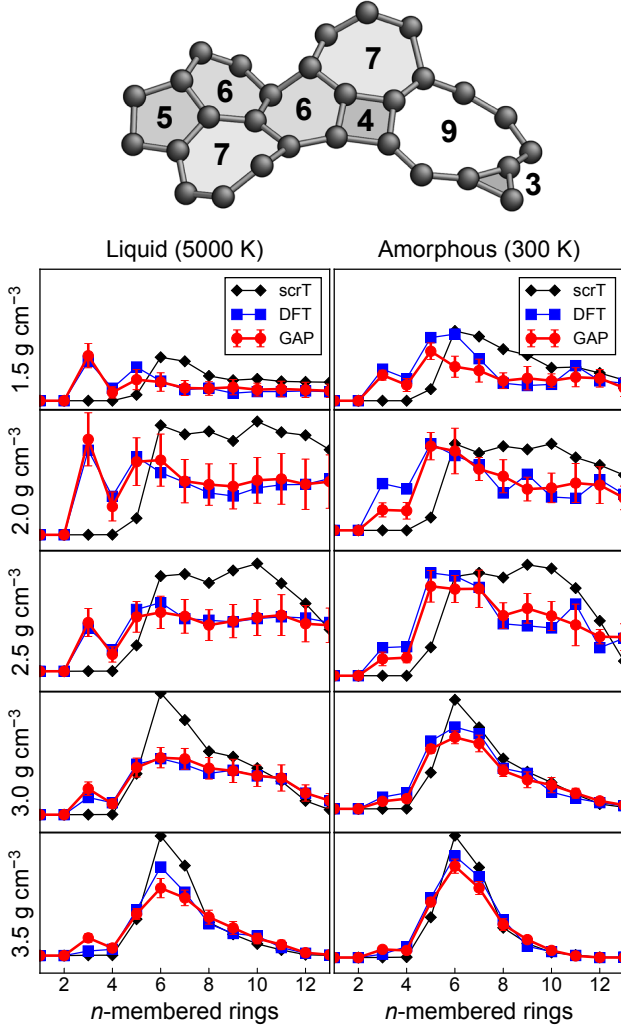


FIG. 11. Medium-range order in a -C as evaluated through ring statistics. *Top*: Structural fragment from one of the DFT generated a -C structures at 2.0 g cm^{-3} , chosen to visualize the diversity of ring sizes observed. Rings are indicated by shading, and their size n is given. *Bottom*: Ring statistics for liquid (*left*) and quenched amorphous (*right*) carbon structures obtained from DFT (blue), GAP (red), and screened Tersoff potential (“scrT”; black) simulations. Data for the liquid structures have been collected over the last 1 ps of the respective trajectory; data for the amorphous structures correspond to the last snapshot only, as the structures are strongly correlated in this case. For GAP-derived structures, the standard deviation for the count of each ring size is indicated by error bars.

the *average* from the 216-atom structures (red). Hence, while a single 216-atom snapshot will not be sufficient to investigate ring statistics of a -C models, one may instead collect averages over sufficiently many smaller structures, and therefore reproduce the short- and medium-range structural features without requiring larger simulation cells. Nonetheless, there *is* an inherent deviation between the 216- and 8000-atom structures: namely, at very large

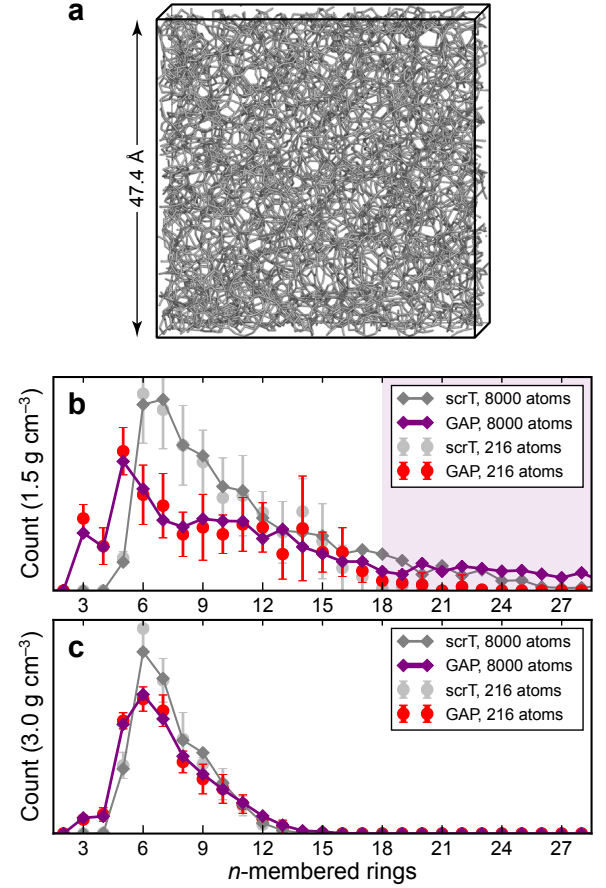


FIG. 12. Application of the GAP to larger-scale simulations. (a) Melt-quenched 8,000-atom structure of a -C at 1.5 g cm^{-3} , shown as stick drawing. (b) Ring statistics for this structure (purple) and as averaged over 10 different 216-atom structures (red; as in Fig. 11). Purple shading emphasizes ring sizes of $n \geq 18$ that the smaller systems cannot reproduce. (c) Same analysis but for ta -C (3.0 g cm^{-3}).

ring sizes ($n \geq 18$; shaded in Fig. 12b), which the 216-atom cells cannot reproduce as they are simply too small. This emphasizes that realistic studies of voids and porosity in a -C will require large structures on the order of at least several thousand atoms.

We also created an 8,000-atom ta -C structure (Fig. 12c): in this case, no voids are found but a dense, “diamond-like” network. Consequently, no large rings ($n > 15$) are observed, and the 216-atom simulations already provide a very good estimate of the medium-range structural order. Likewise, the screened Tersoff potential here correctly reproduces the maximum at $n = 6$ as well as the abundance of larger-membered rings. The latter drops to zero between $n = 12$ and $n = 15$ for all potentials and system sizes investigated.

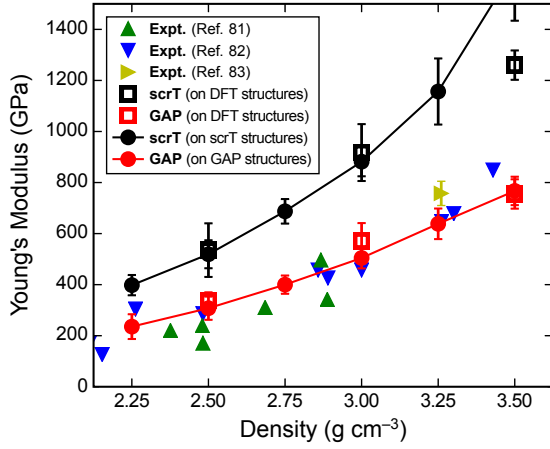


FIG. 13. Young's modulus of *a*-C as a function of density. Experimental values are taken from Ref. 81 (green), Ref. 82 (blue), and Ref. 83 (yellow), respectively. Lines between data points are guides to the eye.

E. Elastic properties

We next evaluated the Young's modulus of *a*-C which, like the sp^3 count, depends strongly on density.^{81–83} We compare results using scrT and GAP, but not DFT, due to the high expense of fully relaxing the internal degrees of freedom for several uncorrelated models. In addition, we disentangle the effect of input structure versus potential performance for the prediction of elastic properties, and therefore also use both scrT and GAP to evaluate the Young's moduli of DFT-generated structures.

To compute the Young's modulus of *a*-C, we take previously generated 216-atom structures, perform further short MD quenches from 300 K to very low temperature, and finally a conjugate-gradient relaxation to minimize the forces on atoms; the cell vectors remain fixed to keep the density unchanged. For each optimized structure, we compute the full 6×6 matrix of elastic constants \mathbf{C} without imposing symmetry operations, and invert this matrix to obtain the compliance matrix \mathbf{S} .⁸⁴ From this, we calculate the Young's modulus E (see, e.g., Ref. 85) by averaging over the three spatial directions:

$$E = \frac{1}{3} \left[\frac{1}{S_{11}} + \frac{1}{S_{22}} + \frac{1}{S_{33}} \right] \quad (13)$$

and subsequently over independent structures (ten from scrT and GAP melt-quench runs, three for the DFT case; see above). The GAP results agree very well with experiments at all relevant densities (Fig. 13), and as expected they predict increased stiffness as density and sp^3 concentration (“diamond-likeness”) increase. The screened Tersoff potential correctly captures the same trend, albeit the absolute values are significantly overestimated; this is most pronounced at higher densities.

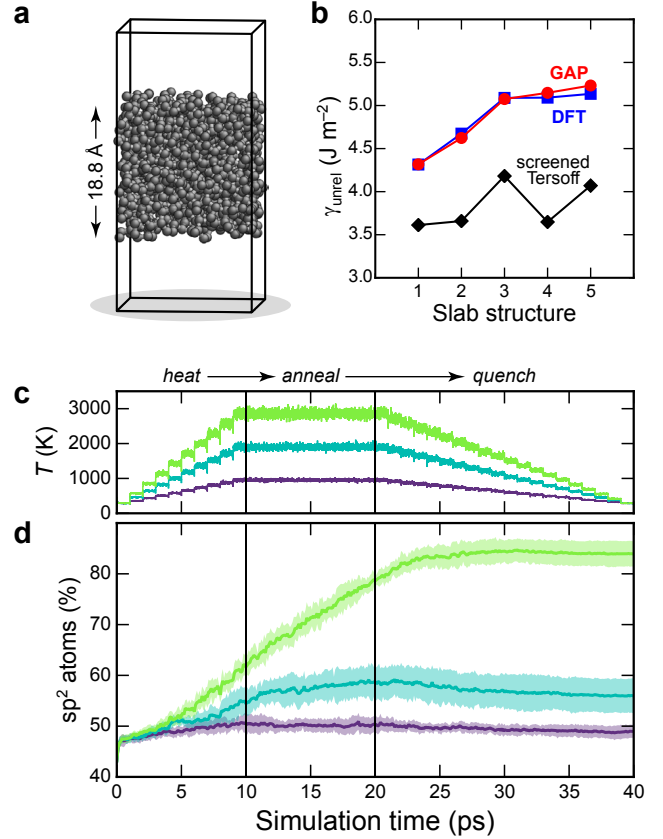


FIG. 14. (a) Exemplary surface slab of *ta*-C, freshly cleaved from a 1000-atom bulk structure. (b) Unrelaxed surface energies (Eq. 14) for five slabs cleaved from the same bulk structure. Lines between data points are guides to the eye. (c) Course of temperatures in the protocol we use to generate reconstructed surfaces: the systems are heated over 10 ps to 1000 (green), 2000 (yellow), or 3000 K (red), respectively, and annealed at this temperature for another 10 ps. The final 20 ps then constitute a slower cooling back to 300 K. (d) Concentration of sp^2 carbon atoms in 1000-atom slabs versus simulation time. Averages over ten independent structures are given, and areas of light shading indicate standard deviations.

F. From the bulk to surfaces

Realistic materials modeling, especially at the nanoscale, must extend from the bulk to a description of crystal surfaces and their reactivity.⁸⁶ Likewise, the surfaces of amorphous matter are of broad interest but pose particular and significant challenges for modeling. We here present initial applications of our GAP to amorphous carbon surfaces of the 3.0 g cm^{-3} phase (*ta*-C). This is because dense, diamond-like carbon is used in coatings⁶ and it is this form for which surface phenomena are most relevant.

Early studies of *ta*-C surfaces have been reported at the DFT level but have necessarily been restricted to very small system sizes.⁸⁷ Larger-scale simulations were made possible by tight-binding schemes⁸⁸ and EDIP,⁸⁹

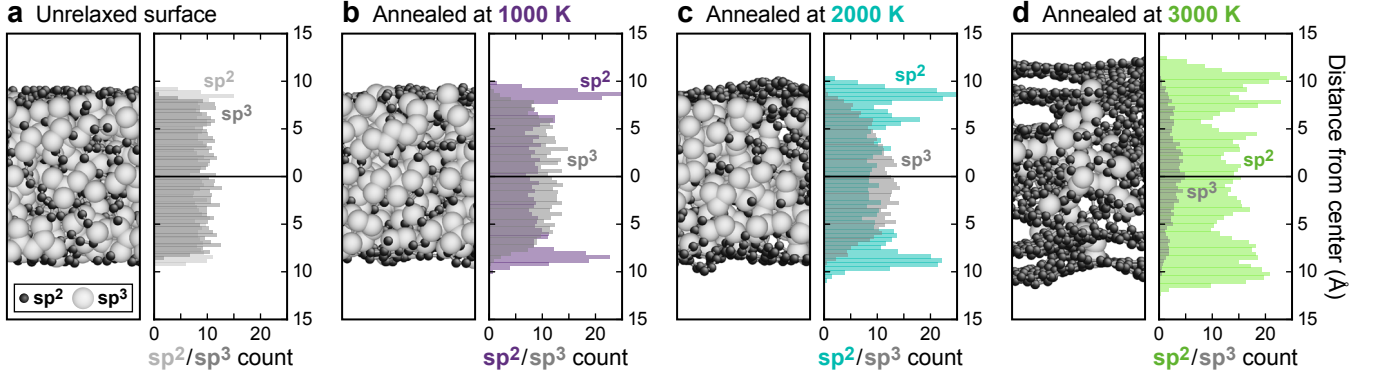


FIG. 15. Surfaces of *ta*-C before (a) and after annealing at different temperatures (b–d) as predicted from GAP simulations. Each panel shows one exemplary slab structure on the left, with sp^2 (“graphite-like”) atoms drawn as small dark spheres, and sp^3 (“diamond-like”) atoms larger and light gray. Note how annealing at 3000 K leads to beginning detachment of graphitic-like sheets, and disintegration of the *ta*-C regions even in the center of the slab. Histograms for the sp^2/sp^3 distribution in direction normal to the surface have been collected over ten independent structures; the count is normalized per simulation cell.

but even high-quality empirical potentials may face problems when it comes to the prediction of surface energies; this has already been reported for diamond.⁷⁴

Conventionally, the surface energy, γ , is calculated as

$$\gamma = \frac{1}{2A} [E_{\text{slab}} - N \times E_{\text{bulk}}] \quad (14)$$

for an elemental (or stoichiometrically precise) surface slab that contains N atoms and exposes equivalent surface areas A at top and bottom; in this expression, E_{slab} denotes computed total energies for a slab model per unit cell, and E_{bulk} refers to the energy of the underlying bulk structure per atom.

For amorphous systems, the structure of the surface is not uniquely defined (there are no distinct cleavage planes as in crystals), and to calculate γ one must average over many large structures. We assess the suitability of the GAP model for such studies by computing surface energies of *ta*-C and comparing to DFT values. We used a GAP to generate a 1000-atom bulk *ta*-C structure and cleaved five different surfaces normal to the [001] direction of the simulation cell (cf. Fig. 14a). For each surface, the unrelaxed surface energy was evaluated using the three methods (Fig. 14b). The GAP model fully reproduces the stability ordering; for the most stable surface (structure 1), GAP and DFT results differ by less than 0.01 J m^{-2} . For the two least stable candidates, 4 and 5, this difference increases slightly but remains small (below 0.1 J m^{-2} , or 2%). The screened Tersoff potential yields much lower surface energies, similar to what has been reported for diamond.⁷⁴

We finally perform high-temperature annealing simulations with our GAP, to assess structural relaxations and reconstructions at *ta*-C surfaces. These are associated with an increased formation of sp^2 atoms (“graphitization”) that has been observed in several *ex-situ* experiments⁹⁰ and also *in situ* during film growth.⁹¹ A discussion of the relevant differences between experiment

and theory has been given by Marks.⁸⁹ Higher temperatures than in experiment must be used to overcome kinetic barriers during simulation—as experiments typically involve up to one hour of annealing.⁹⁰ In that sense, the *absolute* annealing temperature used for simulation is fictitious;⁸⁹ its choice depends on the computational method,⁸ and a suitable annealing temperature must therefore be found by trial and error.

In Fig. 14c–d we explore the use of different such temperatures, and in particular we analyze the structures obtained before and after each of the different annealing runs (Fig. 15). In each simulation, the slab is gradually heated to the target temperature over 10 ps, annealed for 10 ps, and then cooled back to 300 K over another 20 ps; each structure contains 1000 atoms, and ten independent ones are studied in parallel to improve statistics. Monitoring the concentration of sp^2 atoms during these simulations provides the most direct insight: heating to 1000 K induces no significant changes, albeit it “heals” the dangling bonds directly at the surface (indicated by a small jump in sp^2 immediately upon initializing the simulation); therefore, the 1000 K annealed structure may be a useful representative of the *non*-graphitized surface. At the intermediate setting of 2000 K, the sp^2 concentration in the system rises slightly during annealing and is then lowered again during cooling; the interior of the slab and its density remain close to that of bulk *ta*-C, whereas reconstructions are observed at the surface. Finally, heating to 3000 K graphitizes the entire system; this is reminiscent of what was seen earlier by Powles and co-workers using the EDIP model.⁷ It also leads to a strong expansion of the slab interior (Fig. 15d).

A top view best visualizes the atomic-scale processes at the surface (Fig. 16). The freshly cleaved, unrelaxed structure shows a number of “dangling bonds” and low-coordinated atoms, trivially so as the tetrahedra in *ta*-C have been cut apart. These defects largely disappear

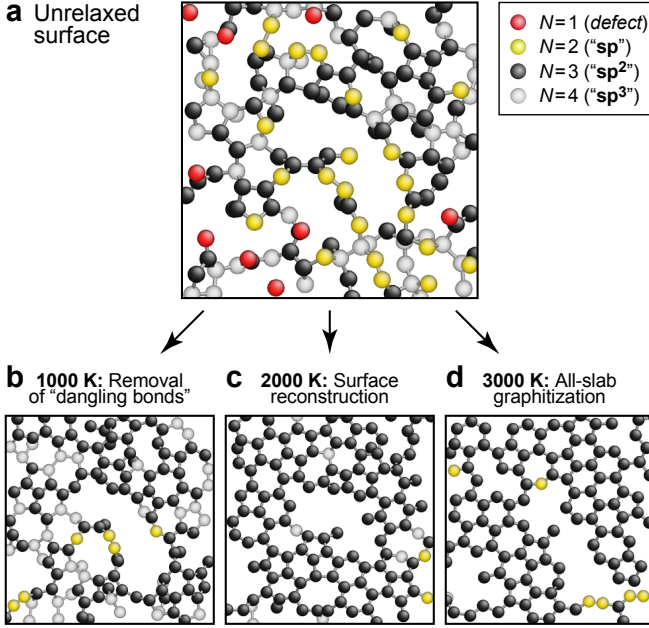


FIG. 16. Top views of the same surface structure before (a) and after (b–d) different degrees of annealing. Only atoms in the outermost 3 Å are shown, and coloring indicates the coordination number.

during annealing at 1000 K already, but at this temperature the surface stays strongly disordered (Fig. 16b). By contrast, increasing the annealing temperature to 2000 K leads to graphitized layers of several Å thickness at the surfaces (Fig. 15c): sixfold rings are seen, as well as pairs of five- and sevenfold ones that are likely metastable (Fig. 16c); still, the surface atoms are connected to lower-lying sp³ atoms even within the topmost 3 Å, and the graphitization therefore remains a genuine surface phenomenon. By contrast, during annealing at 3000 K, the entire slab graphitizes as seen above, and a strongly defective graphene sheet begins to detach from the surface; no near-surface sp³ atoms are seen any more (Fig. 16d).

V. CONCLUSIONS

We have developed a machine-learning based GAP model for atomistic simulations of liquid and amorphous elemental carbon. The structural complexity that the potential has to encompass, as well as the nonlocality in forces are notable, and larger than in any previous ML-based interatomic potential model. Nonetheless, our GAP predicts energies that are largely in the range of tens of meV/atom; characteristic structural properties, such as the sp³ count and the medium-range order as expressed through ring statistics, are faithfully recovered, and surface energies and reconstructions are well described by the GAP.

The central issue in the development of atomistic materials modeling remains in the tradeoff between accuracy and cost. The GAP model presented here is many orders of magnitude faster than DFT, but slower than state-of-the-art empirical potentials (while similarly linear scaling). Being thus intermediate between both realms, GAP models appear to be promising tools for accurate large-scale atomistic simulations, including amorphous materials and their surfaces.

ACKNOWLEDGMENTS

We thank L. Pastewka, A. P. Bartók, J. R. Kermode, and S. R. Elliott for ongoing valuable discussions and for helpful remarks on this work. V.L.D. gratefully acknowledges a postdoctoral fellowship from the Alexander von Humboldt Foundation, as well as support from the Isaac Newton Trust (Trinity College Cambridge). This work used the ARCHER UK National Supercomputing Service (<http://www.archer.ac.uk>) via EPSRC Grant EP/K014560/1.

* vld24@cam.ac.uk

¹ A. Hirsch, Nat. Mater. **9**, 868 (2010).

² V. Georgakilas, J. A. Perman, J. Tucek, and R. Zboril, Chem. Rev. **115**, 4744 (2015).

³ R. Hoffmann, A. A. Kabanov, A. A. Golov, and D. M. Proserpio, Angew. Chem. Int. Ed. **55**, 10962 (2016).

⁴ D. R. McKenzie, D. Muller, and B. A. Pailthorpe, Phys. Rev. Lett. **67**, 773 (1991).

⁵ D. R. McKenzie, Rep. Prog. Phys. **59**, 1611 (1999).

⁶ J. Robertson, Mater. Sci. Eng. R Reports **37**, 129 (2002).

⁷ R. C. Powles, N. A. Marks, and D. W. M. Lau, Phys. Rev. B **79**, 075430 (2009).

⁸ C. de Tomas, I. Suarez-Martinez, and N. A. Marks, Carbon **109**, 681 (2016).

⁹ J. Li, Model. Simul. Mater. Sci. Eng. **11**, 173 (2003).

¹⁰ For an overview, see: N. A. Marks, in *Computer-Based Modeling of Novel Carbon Systems and Their Properties: Beyond Nanotubes*, eds. L. Colombo, A. Fasolino (Springer, Dordrecht, 2010), pp. 129–169.

¹¹ J. Tersoff, Phys. Rev. Lett. **61**, 2879 (1988).

¹² D. W. Brenner, Phys. Rev. B **42**, 9458 (1990).

¹³ N. A. Marks, Phys. Rev. B **63**, 035401 (2000).

¹⁴ D. W. Brenner, O. A. Shenderova, J. A. Harrison, S. J. Stuart, B. Ni, and S. B. Sinnott, J. Phys.: Condens. Matter **14**, 783 (2002).

¹⁵ L. Pastewka, P. Pou, R. Pérez, P. Gumbsch, and M. Moseler, Phys. Rev. B **78**, 161402 (2008).

¹⁶ S. G. Srinivasan, A. C. T. van Duin, and P. Ganesh, J. Phys. Chem. A **119**, 571 (2015).

¹⁷ B. D. Jensen, K. E. Wise, and G. M. Odegard, J. Phys.

- Chem. A **119**, 9710 (2015).
- ¹⁸ L. Pastewka, S. Moser, and M. Moseler, *Tribol. Lett.* **39**, 49 (2010); L. Pastewka, S. Moser, P. Gumbsch, and M. Moseler, *Nat. Mater.* **10**, 34 (2011).
 - ¹⁹ N. Marks, *J. Phys.: Condens. Matter* **14**, 2901 (2002), and references therein.
 - ²⁰ C. Z. Wang and K. M. Ho, *Phys. Rev. Lett.* **71**, 1184 (1993); *Phys. Rev. B* **50**, 12429 (1994).
 - ²¹ T. Frauenheim, P. Blaudeck, U. Stephan, and G. Jungnickel, *Phys. Rev. B* **48**, 4823 (1993).
 - ²² T. Köhler, T. Frauenheim, and G. Jungnickel, *Phys. Rev. B* **52**, 11837 (1995).
 - ²³ G. Galli, R. M. Martin, R. Car, and M. Parrinello, *Phys. Rev. Lett.* **62**, 555 (1989).
 - ²⁴ D. A. Drabold, P. A. Fedders, and P. Stumm, *Phys. Rev. B* **49**, 16415 (1994).
 - ²⁵ N. A. Marks, D. R. McKenzie, B. A. Pailthorpe, M. Bernasconi, and M. Parrinello, *Phys. Rev. Lett.* **76**, 768 (1996).
 - ²⁶ D. G. McCulloch, D. R. McKenzie, and C. M. Goringe, *Phys. Rev. B* **61**, 2349 (2000).
 - ²⁷ F. Risplendi, M. Bernardi, G. Cicero, and J. C. Grossman, *Appl. Phys. Lett.* **105**, 043903 (2014).
 - ²⁸ D. Music, R. W. Geyer, and J. M. Schneider, *Surf. Coat. Technol.* **286**, 178 (2016).
 - ²⁹ X. Wang, S. Scandolo, and R. Car, *Phys. Rev. Lett.* **95**, 185701 (2005).
 - ³⁰ S. Lorenz, A. Groß, and M. Scheffler, *Chem. Phys. Lett.* **395**, 210 (2004).
 - ³¹ J. Behler and M. Parrinello, *Phys. Rev. Lett.* **98**, 146401 (2007).
 - ³² N. Artrith and A. Urban, *Comput. Mater. Sci.* **114**, 135 (2016).
 - ³³ A. Seko, A. Takahashi, and I. Tanaka, *Phys. Rev. B* **92**, 054113 (2015).
 - ³⁴ A. P. Bartók, M. C. Payne, R. Kondor, and G. Csányi, *Phys. Rev. Lett.* **104**, 136403 (2010).
 - ³⁵ H. Eshet, R. Z. Khaliullin, T. D. Kühne, J. Behler, and M. Parrinello, *Phys. Rev. B* **81**, 184107 (2010).
 - ³⁶ R. Z. Khaliullin, H. Eshet, T. D. Kühne, J. Behler, and M. Parrinello, *Phys. Rev. B* **81**, 100103 (2010).
 - ³⁷ N. Artrith, T. Morawietz, and J. Behler, *Phys. Rev. B* **83**, 153101 (2011).
 - ³⁸ N. Artrith and J. Behler, *Phys. Rev. B* **85**, 045439 (2012).
 - ³⁹ W. J. Szlachta, A. P. Bartók, and G. Csányi, *Phys. Rev. B* **90**, 104108 (2014).
 - ⁴⁰ J. Behler, R. Martonák, D. Donadio, and M. Parrinello, *Phys. Rev. Lett.* **100**, 185501 (2008); R. Z. Khaliullin, H. Eshet, T. D. Kühne, J. Behler, and M. Parrinello, *Nat. Mater.* **10**, 693 (2011).
 - ⁴¹ M. Rupp, A. Tkatchenko, K.-R. Müller, and O. A. von Lilienfeld, *Phys. Rev. Lett.* **108**, 058301 (2012); F. A. Faber, A. Lindmaa, O. A. von Lilienfeld, and R. Armiento, *Phys. Rev. Lett.* **117**, 135502 (2016).
 - ⁴² M. G. Darley, C. M. Handley, and P. L. A. Popelier, *J. Chem. Theory Comput.* **4**, 1435 (2008); C. M. Handley, G. I. Hawe, D. B. Kell, and P. L. A. Popelier, *Phys. Chem. Chem. Phys.* **11**, 6365 (2009).
 - ⁴³ J. Lee, A. Seko, K. Shitara, K. Nakayama, and I. Tanaka, *Phys. Rev. B* **93**, 115104 (2016).
 - ⁴⁴ M. Rupp, R. Ramakrishnan, and O. A. von Lilienfeld, *J. Phys. Chem. Lett.* **6**, 3309 (2015); J. Cuny, Y. Xie, C. J. Pickard, and A. A. Hassanali, *J. Chem. Theory Comput.* **12**, 765 (2016).
 - ⁴⁵ M. Rupp, *Int. J. Quantum Chem.* **115**, 1058 (2015).
 - ⁴⁶ G. C. Sosso, G. Miceli, S. Caravati, J. Behler, and M. Bernasconi, *Phys. Rev. B* **85**, 174103 (2012).
 - ⁴⁷ G. C. Sosso, D. Donadio, S. Caravati, J. Behler, and M. Bernasconi, *Phys. Rev. B* **86**, 104301 (2012).
 - ⁴⁸ G. C. Sosso, G. Miceli, S. Caravati, F. Giberti, J. Behler, and M. Bernasconi, *J. Phys. Chem. Lett.* **4**, 4241 (2013).
 - ⁴⁹ S. R. Elliott, *Nature* **354**, 445 (1991).
 - ⁵⁰ J. Akola and R. O. Jones, *Phys. Stat. Sol. B* **249**, 1851 (2012); W. Zhang, V. L. Deringer, R. Dronskowski, R. Mazzarello, E. Ma, and M. Wuttig, *MRS Bull.* **40**, 856 (2015).
 - ⁵¹ A. P. Bartók and G. Csányi, *Int. J. Quantum Chem.* **115**, 1051 (2015).
 - ⁵² A. P. Bartók, R. Kondor, and G. Csányi, *Phys. Rev. B* **87**, 184115 (2013).
 - ⁵³ J. Behler, *Phys. Chem. Chem. Phys.* **13**, 17930 (2011).
 - ⁵⁴ Z. Li, J. R. Kermode, and A. De Vita, *Phys. Rev. Lett.* **114**, 096405 (2015).
 - ⁵⁵ V. Botu and R. Ramprasad, *Phys. Rev. B* **92**, 094306 (2015).
 - ⁵⁶ A. Shapeev, *Multiscale Model. Simul.* **14**, 1153 (2016).
 - ⁵⁷ P. E. Dolgirev, I. A. Kruglov, and A. R. Oganov, *AIP Adv.* **6**, 085318 (2016).
 - ⁵⁸ S. De, A. P. Bartók, G. Csányi, and M. Ceriotti, *Phys. Chem. Chem. Phys.* **18**, 13754 (2016).
 - ⁵⁹ M. J. Cliffe, A. P. Bartók, R. N. Kerber, C. P. Grey, G. Csányi, and A. L. Goodwin, *arXiv:1609.00668* (2016).
 - ⁶⁰ G. Bussi, D. Donadio, and M. Parrinello, *J. Chem. Phys.* **126**, 014101 (2007).
 - ⁶¹ J. VandeVondele, M. Krack, F. Mohamed, M. Parrinello, T. Chassaing, and J. Hutter, *Comput. Phys. Commun.* **167**, 103 (2005); J. Hutter, M. Iannuzzi, F. Schiffmann, and J. VandeVondele, *Wiley Interdiscip. Rev.—Comput. Mol. Sci.* **4**, 15 (2014); www.cp2k.org.
 - ⁶² T. D. Kühne, M. Krack, F. R. Mohamed, and M. Parrinello, *Phys. Rev. Lett.* **98**, 066401 (2007).
 - ⁶³ S. Goedecker, M. Teter, and J. Hutter, *Phys. Rev. B* **54**, 1703 (1996).
 - ⁶⁴ W. Kohn and L. J. Sham, *Phys. Rev.* **140**, A1133 (1965).
 - ⁶⁵ S. J. Clark, M. D. Segall, C. J. Pickard, P. J. Hasnip, M. J. Probert, K. Refson, and M. C. Payne, *Z. Krist.* **220**, 567 (2005).
 - ⁶⁶ H. J. Monkhorst and J. D. Pack, *Phys. Rev. B* **13**, 5188 (1976).
 - ⁶⁷ G. P. Francis and M. C. Payne, *J. Phys. Condens. Matter* **2**, 4395 (1990).
 - ⁶⁸ This can even turn out as an advantage—namely, if two techniques lead to different and simultaneously relevant regions of configuration space.
 - ⁶⁹ M. W. Mahoney and P. Drineas, *Proc. Natl. Acad. Sci. U. S. A.* **106**, 697 (2009).
 - ⁷⁰ W. Kohn, *Phys. Rev. Lett.* **76**, 3168 (1996).
 - ⁷¹ F. Q. Nazar and C. Ortner, *arXiv:1509.06753* (2016).
 - ⁷² For the locality tests, we used CASTEP as described in the Methods section; the reciprocal-space grids were reduced to make the computational workload tractable.
 - ⁷³ One is tempted to correlate this with the more metallic nature of lower-density *a*-C (see, e.g., Ref. 27); a definitive answer would require sampling over a much larger number of structures, though, especially given the large error bars involved.
 - ⁷⁴ L. Pastewka, A. Klemenz, P. Gumbsch, and M. Moseler, *Phys. Rev. B* **87**, 205410 (2013).

- ⁷⁵ A. Klemenč, L. Pastewka, S. G. Balakrishna, A. Caron, R. Bennwitz, and M. Moseler, *Nano Lett.* **14**, 7145 (2014).
- ⁷⁶ T. Kunze, M. Posselt, S. Gemming, G. Seifert, A. R. Koniczek, R. W. Carpick, L. Pastewka, and M. Moseler, *Tribol. Lett.* **53**, 119 (2014).
- ⁷⁷ P. J. Fallon, V. S. Veerasamy, C. A. Davis, J. Robertson, G. A. J. Amaratunga, W. I. Milne, and J. Koskinen, *Phys. Rev. B* **48**, 4777 (1993).
- ⁷⁸ J. Schwan, S. Ulrich, H. Roth, H. Ehrhardt, S. R. P. Silva, J. Robertson, R. Samlenski, and R. Brenn, *J. Appl. Phys.* **79**, 1416 (1996).
- ⁷⁹ A. C. Ferrari, A. Libassi, B. K. Tanner, V. Stolojan, J. Yuan, L. M. Brown, S. E. Rodil, B. Kleinsorge, and J. Robertson, *Phys. Rev. B* **62**, 11089 (2000).
- ⁸⁰ D. S. Franzblau, *Phys. Rev. B* **44**, 4925 (1991).
- ⁸¹ B. Schultrich, H.-J. Scheibe, G. Grandremy, D. Drescher, and D. Schneider, *Diam. Relat. Mater.* **5**, 914 (1996).
- ⁸² B. Schultrich, H.-J. Scheibe, D. Drescher, and H. Ziegele, *Surf. Coatings Technol.* **98**, 1097 (1998).
- ⁸³ A. C. Ferrari, J. Robertson, M. G. Beghi, C. E. Bottani, R. Ferulano, and R. Pastorelli, *Appl. Phys. Lett.* **75**, 1893 (1999).
- ⁸⁴ J. F. Nye, *Physical Properties of Crystals: Their Presentation by Tensors and Matrices* (Clarendon, Oxford, 1969).
- ⁸⁵ W. A. Brantley, *J. Appl. Phys.* **44**, 534 (1973).
- ⁸⁶ V. L. Deringer and R. Dronskowski, *Angew. Chem. Int. Ed.* **54**, 15334 (2015), and references therein.
- ⁸⁷ J. Dong and D. A. Drabold, *Phys. Rev. B* **57**, 15591 (1998); C. Chen and J. Robertson, *Diam. Relat. Mater.* **15**, 936 (2006); C. W. Bauschlicher, Jr. and J. W. Lawson, *Chem. Phys.* **374**, 77 (2010); M. A. Caro, R. Zoubkoff, O. Lopez-Acevedo, and T. Laurila, *Carbon* **77**, 1168 (2014).
- ⁸⁸ R. Haerle, G. Galli, and A. Baldereschi, *Appl. Phys. Lett.* **75**, 1718 (1999).
- ⁸⁹ N. A. Marks, M. F. Cover, and C. Kocer, *Appl. Phys. Lett.* **89**, 131924 (2006); N. Marks, M. Cover, and C. Kocer, *Mol. Simul.* **32**, 1271 (2006).
- ⁹⁰ T. A. Friedmann, K. F. McCarty, J. C. Barbour, M. P. Siegal, and D. C. Dibble, *Appl. Phys. Lett.* **68**, 1643 (1996); J. P. Sullivan, T. A. Friedmann, and A. G. Baca, *J. Electron. Mater.* **26**, 1021 (1997); A. C. Ferrari, B. Kleinsorge, N. A. Morrison, A. Hart, V. Stolojan, and J. Robertson, *J. Appl. Phys.* **85**, 7191 (1999).
- ⁹¹ M. Chhowalla, J. Robertson, C. W. Chen, S. R. P. Silva, C. A. Davis, G. A. J. Amaratunga, and W. I. Milne, *J. Appl. Phys.* **81**, 139 (1997).

Supplementary Information

COMPOSITION OF TRAINING DATABASE

The database is kept in extended xyz format, which allows us to store data for atomic positions and forces, as well as total energies and virials, all in the same file. Individual configurations are concatenated, and identified by two custom keywords, `config_type` and `detailed_ct`, respectively. The first is used for grouping the data during training. The second, more detailed configuration type indicates how exactly the training data have been obtained. A description is provided in the following.

For all parts of the dataset, the number of points given here refers to the structures that in the (randomly sampled) *training set*, which comprised 90% of the total database. For example, for the “`step0`” dataset, a total of 500 structures were computed, and from these a random number generator selected 462 entries for the training and 38 entries for the test set.

Bulk liquid and amorphous carbon structures (`config_type=bulk_amo`)

- `detailed_ct=step0` (462 points, 64 at./cell): Liquid carbon at 9000 K; five `cp2k` trajectories at densities of 1.5, 2.0, 2.5, 3.0, and 3.5 g cm⁻³, respectively. Each trajectory had 3000 steps, from which every 30 steps a snapshot was taken and added to the database.
- `detailed_ct=LDL` (166 points, 64 at./cell): Low-density liquid: additional `cp2k` snapshots at densities of 1.50 and 2.00 g cm⁻³, taken both at 9000 K and 5000 K. These were added at an intermediate stage during training, to prevent the GAP from predicting too many “sp” chains in the low-density liquids.
- `detailed_ct=qu_cp2k` (88 points, 64 at./cell): Liquid structures created with a preliminary GAP (trained on `step0`) that were then equilibrated at 5000 K (0.5 ps) and quenched (0.5 ps) to 300 K using `cp2k`. Ten uncorrelated structures were generated at 2.0 cm⁻³, and ten at 3.0 cm⁻³.
- `detailed_ct=qu_tetra` (107 points, 64 at./cell): Melt-quench trajectories with a focus on higher densities (richer in tetrahedral motifs). We repeated the above for high-density structures, generating ten structures each at 3.25 and 3.5 g/cm⁻³, respectively; this was done to include structures more rich in tetrahedra early on.
- Iterative training: Iteration 2
 - `detailed_ct=iter2.1` (274 points, 27–64 at./cell): Using an intermediate GAP (with distance, angle, and SOAP descriptors, the latter employing 1000 sparse points; hence denoted `das1000`), trained using a part of the above data, 100 independent melt-quench trajectories were performed with randomized densities between 1.5 and 3.5 g cm⁻³. From each, three structures were extracted: one from the equilibrated 5000 K liquid (at 6.00 ps), one during the quench (at 6.15 ps), and one final step representing the equilibrated amorphous phase (at 9.50 ps). For each, a single-point computation was performed and added to the database.
- `detailed_ct=iter2.2` (86 points, 27–64 at./cell): Same but using a GAP model with a larger number of SOAP sparse points (`das2000`); 100 independent trajectories from each of which only the final step was taken.
- `detailed_ct=iter2.3` (186 points, 64 at./cell): As before but using a smaller GAP model (`das0250`); 200 independent melt-quench trajectories from each of which only the final step was taken.
- `detailed_ct=iter2.4` (272 points, 64–125 at./cell): Starting structures increased to include 4 × 4 × 5 (80 at.), 4 × 5 × 5 (100 at.), and 5 × 5 × 5 (125 at.) expansions.
- Iterative training: Iteration 3
 - `detailed_ct=iter3.1` (260 points, 27–64 at./cell): Using the previous data including the second iteration, a new GAP model was fitted and this was in turn used to generate structures as described for `iter2.1`.
 - `detailed_ct=iter3.2` (87 points, 27–64 at./cell): As before, but with a GAP model using slightly modified parameters compared to `iter3.1`; in this case, only the last step from each trajectory was used.
- Iterative training: Iteration 4
 - `detailed_ct=iter4.1` (272 points, 27–64 at./cell): Iterative training as before, generating structures as described for `iter2.1`.
 - `detailed_ct=iter4.2` (356 points, 27–64 at./cell): Iterative training as before, generating structures as described for `iter2.1`, with slightly modified GAP parameters compared to `iter4.1`.
- Iterative training: Iteration 5
 - `detailed_ct=iter5.1` (178 points, 125 at./cell): Iterative training as before, now increasing the system size; 100 independent melt-quench runs were performed, from which one snapshot from the 9000 K liquid and one from the amorphous structure was taken.
 - `detailed_ct=iter5.2` (178 points, 125 at./cell): As before, but using one snapshot from the 5000 K liquid and one during quenching. In total, four structures were thus extracted from each 125-atom melt-quench trajectory.
- `detailed_ct=iter6.1` (91 points, 64 at./cell): Iterative training as before. In this case, once the amorphous structures had been generated, the lattice parameters of the simulation cells were scaled uniformly by a randomized factor between 0.95 and 1.02 (to sample structures further away from equilibrium); subsequently,

the atomic positions were relaxed using a conjugate-gradient scheme, and both scaled unrelaxed and scaled relaxed structures were added to the training database.

- `detailed_ct=iter7_1` (88 points, 64 at./cell): Iterative training as before. In this case, amorphous structures were generated and relaxed, and then one of the lattice parameters was scaled by a randomized factor between 0.95 and 1.05; this strained cell was then added to the database.

Amorphous surfaces (`config.type=surf_amo`)

- `detailed_ct=asurf_cp2k_from5k` (274 points, 64 at./cell): Two bulk liquid structures generated with `cp2k` (64 atoms each) were cleaved at five equidistant planes to generate ten slabs in total; each of the latter was subjected to 3 ps of `cp2k` MD at 1000, 2000, and 5000 K in parallel. This leads to highly disordered surface structures with beginning disintegration, and therefore allows us to sample a large diversity of near-surface structures. In total, 30 runs were hence performed, from which ten structures (every 300 steps) were extracted and added to the training database.
- `detailed_ct=surf_from_iter4_216` (81 points, 216 at./cell): Bulk 216-atom *ta*-C structures (3.0 g cm^{-3}) were created, and subsequently cleaved to yield surface slabs; the latter (but not the bulk structures) were added to the database.
- `detailed_ct=surf_unrel_iter4` (92 points, 64 at./cell): Bulk 64-atom *ta*-C structures were cleaved normal to [001], and these slab structures were added to the database.
- `detailed_ct=surf_unrel_iter4_x` (91 points, 64 at./cell): Same but with cleavage normal to [100].
- `detailed_ct=surf_unrel_iter4_y` (86 points, 64 at./cell): Same but with cleavage normal to [010].

Bulk crystal structures (`config.type=bulk_cryst`)

- `detailed_ct=dist_dia` (182 points, 8 at./cell): Distorted configurations starting from the DFT-optimized structure of diamond. We generated 50 structures each with all lattice parameters scaled by factors of 0.94, 0.97, 1.00, or 1.03. For each cell, none, one, or more of the lattice parameters were randomly changed by $\pm 5\%$, and none, one, or more of the angles was randomly changed by ± 5 degrees; the other parameters were kept fixed. The atomic positions in each cell were randomly either (i) fixed, (ii) displaced randomly by $\pm 0.02 \text{ \AA}$, or (iii) relaxed using the Tersoff potential.
- `detailed_ct=dist_graphite` (174 points): Same as above, but for graphite.

Isolated dimer (`config.type=cluster`)

- `detailed_ct=dimer` (30 points, 4 at./cell): DFT computations for C_2 dimers with bond lengths of 0.8–3.7 \AA (in increments of 0.1 \AA). In this case, a large cell of $20 \times 15 \times 15 \text{ \AA}^3$ was used, and reciprocal space was sampled at Γ .

ERRORS FOR TEST VERSUS TRAINING SET

To test the performance of an ML potential outside its training range, it has been advocated to take a certain subset from the structural database as “test set” that is not included in the training. Here, doing so evidences that the errors in both subsets are practically superimposable (Fig. S1): this is encouraging with regard to the quality of the potential, but also to the completeness of the underlying database, as the test set is randomly drawn from the training data and hence structurally similar to them. In other words, Fig. S1 addresses not the extrapolation but the *interpolation* behavior of our GAP.

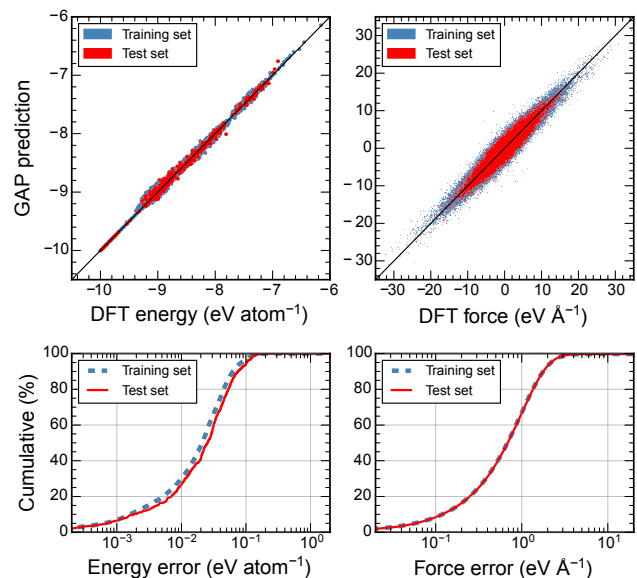


FIG. S1. Scatterplot of DFT-computed and GAP-predicted total energies and force components for all 4050 structural models in the training set (*blue*) and for a separate test set of 450 structures (*red*) not included in the training. Below, the cumulative error distributions are given, which are very close for the energies, and practically indistinguishable for the force components.

TRIMER POTENTIALS

Albeit the GAP model reported here is trained for bulk and surface (that is, extended) structures, we performed additional tests for isolated trimers to assess the extrapolation behavior of the GAP. This case study allows us to more clearly pinpoint the effect of different training data, and the large improvement in potential quality that can be achieved by including dimer data during the fit.

Therefore, we place two carbon atoms in a large box, at a fixed distance of $d(\text{C} - \text{C}) = 1.5, 2.0$, or 2.5 \AA . We then place a third atom in the box on finely meshed grid points; the energy of each system is then evaluated as

$$\Delta E = E(\text{trimer}) - E(\text{dimer}) - E(\text{atom}). \quad (15)$$

These interaction energies are characterized in Fig. S2 and compared to DFT reference data. A GAP model for which the fit did not include any dimer or trimer data (leftmost column) shows erroneous extrapolation, including an energy barrier at intermediate distances; no such barrier is seen in DFT. A GAP model fitted to dimer but not to trimer training data reproduces the trimer potential-energy surface qualitatively very well; however, small deviations remain (middle column). We finally tested the performance of a model where the DFT datapoints for the trimer *have* been included during training: not surprisingly, this improves the description of the trimer further.

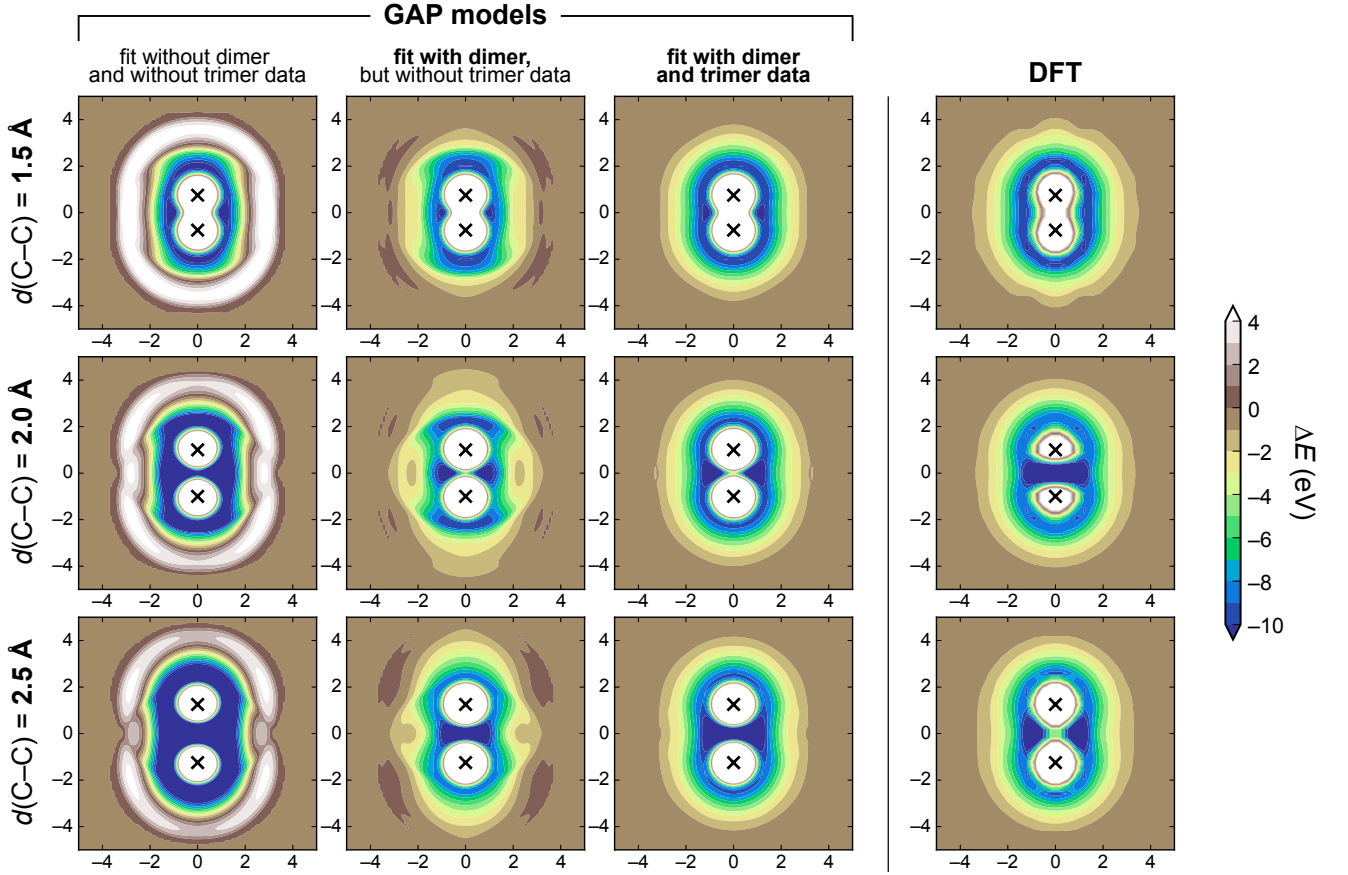


FIG. S2. Potential-energy scans for isolated carbon trimers, computed using different GAP models (left-hand side) and DFT (right-hand side). Two carbon atoms (marked as \times) are placed in the center of a simulation box, and a third atom is placed on finely meshed grid points in the surrounding; at each point, the energy is computed relative to a free “ $\times \times$ ” dimer at the given spacing plus a free atom. (In other words, as soon as the third atom is outside the cutoff radius for both central carbon atoms, the energy drops to zero.)

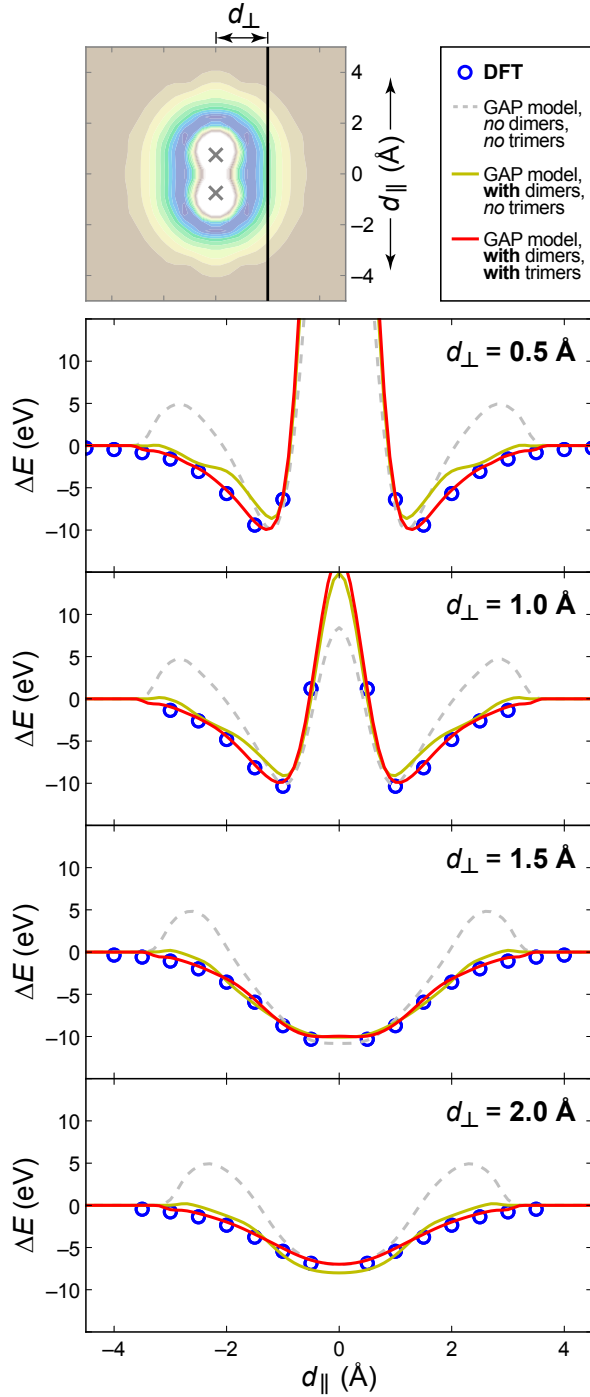


FIG. S3. Line cuts through the datasets shown in the above colormaps: relative energies are given for a line parallel to the dimer ($\times - \times$) bond axis, and for different spacings perpendicular to this bond axis (see schematic at the top left for definitions). The C-C distance in the central dimer is 1.5 Å. Blue symbols show DFT data points, whereas lines denote GAP results; these have been fitted using DFT data for the extended structures only (*dashed gray line*), using a dataset including dimers but not trimers (as in the main text; *yellow*), and finally using a dataset that includes DFT data for both dimers and trimers (*red*).